

The HyLight model for hydrogen emission lines in simulated nebulae

Yuankang Liu  ^{1,2}★ Tom Theuns  ¹ Tsang Keung Chan  ^{3,4} Alexander J. Richings  ^{5,6} and Anna F. McLeod  ^{2,1}

¹ Institute for Computational Cosmology, Department of Physics, Durham University, South Road, Durham DH1 3LE, UK

² Centre for Extragalactic Astronomy, Department of Physics, Durham University, South Road, Durham DH1 3LE, UK

³ Department of Physics, The Chinese University of Hong Kong, Shatin, Hong Kong, China

⁴ Department of Astronomy and Astrophysics, the University of Chicago, Chicago, IL 60637, USA

⁵ Centre for Data Science, Artificial Intelligence and Modelling, University of Hull, Cottingham Road, Hull, HU6 7RX, UK

⁶ E.A. Milne Centre for Astrophysics, University of Hull, Cottingham Road, Hull HU6 7RX, UK

Accepted XXX. Received YYY; in original form ZZZ

ABSTRACT

Hydrogen recombination lines are key diagnostics of ionized gas in the interstellar medium (ISM), particularly within photoionized nebulae. Hydrodynamical simulations, even those that include radiative transfer, do not usually determine the level population of hydrogen required to compute line intensities, but rather interpolate them from pre-computed tables. Here we present the HyLight atomic model, which captures the dominant processes governing the level populations, enabling the calculation of all dipole-allowed hydrogen transitions as well as two-photon transitions from the $2s$ to $1s$ state without the need to pre-compute tables. We compare HyLight predictions to those of other codes and published tables, finding differences between the various rates of up to factors of several per cent for common transitions, including those of the Balmer and Brackett series. However, we find sub-per cent agreement between HyLight and the Cloudy spectral synthesis code when enforcing photo-ionisation equilibrium in gas under typical nebular conditions of density and temperature. Importantly, HyLight can also predict emissivities if the gas is not in photo-ionisation equilibrium. As examples, we compute the ratios between the total photo-ionisation rate and line intensities in a nebula, and post-process a snapshot from SPARCS, a hydrodynamical code that combines radiative transfer with non-equilibrium physics, and compute mock hydrogen emission line maps which can be compared directly to observations. Implemented in PYTHON, HyLight is an accurate tool for determining the level population in neutral hydrogen, a crucial step in bridging the gap between simulations and observations in studies of photoionized regions in galaxies.

Key words: atomic processes – galaxies: ISM – ISM: lines and bands – radiative transfer – methods: numerical hydrodynamics – emission lines

1 INTRODUCTION

Nebular emission lines play a crucial role in determining the physical conditions in star-forming regions and the interstellar medium (ISM) of galaxies (see, for example, the review by Kewley et al. 2019). Physical properties inferred from such lines include the composition (‘metallicity’) of the gas (e.g. Kewley & Dopita 2002; Marino et al. 2013; Perez-Montero 2014; Pérez-Montero 2017), or its electron density, temperature, and pressure (e.g. Seaton & Osterbrock 1957; Peimbert 1967; Rubin 1989). These studies are often based on the ‘Baldwin-Phillips-Terlevich diagram’ (the BPT diagram, Baldwin et al. 1981), which uses the ratios of $[\text{O III}] \lambda 5007/\text{H}\beta$ vs $[\text{N II}] \lambda 6583/\text{H}\alpha$ emission lines to distinguish star-forming galaxies from AGN-dominated galaxies (see e.g. Veilleux & Osterbrock 1987; Kewley et al. 2001; Kauffmann et al. 2003). Other recent examples of using emission line diagnostics include McLeod et al. (2015),

who used the BPT diagram to analyse MUSE¹ integral field unit (IFU) data from VLT of the ‘Pillars of Creation’. McLeod et al. (2019) conducted spatially resolved ionised gas studies in the Large Magellanic Cloud (LMC) using emission line ratios. McLeod et al. (2021) used emission line ratios to distinguish between H II regions, supernova remnants, and planetary nebulae. Isobe et al. (2025) and Shapley et al. (2025) analysed line-ratio diagrams to study the nature of star formation in galaxies at redshifts 3 – 7 observed by the James Webb Space Telescope. Groves et al. (2023) analysed thousands of H II regions in 19 nearby main-sequence galaxies with the help of the bright emission lines. Kennicutt (1998) reviews the use of emission lines to infer star formation rates.

Connecting the physical properties of the nebular gas to the luminosity of its emission lines requires detailed modelling of a range of physical processes, from computing how photons travel through the gas and dust (radiative transfer, henceforth RT), accounting for the impact of collisions on the ionization and excitation state of

★ E-mail: yuankang.liu@durham.ac.uk (YKL)

¹ <https://www.eso.org/sci/facilities/develop/instruments/muse.html>

ions, and finally relating excitation states to emissivity. Two examples of spectral synthesis codes that model these processes include MAPPINGS-v (Sutherland et al. 2018, detailed in Dopita & Sutherland 1996) and CLOUDY (Ferland et al. 1999, recently described in Ferland et al. 2017; Gunasekera et al. 2023). Both include very detailed atomic/molecular physics models and RT, and can be used with relatively simple nebular geometries and situations in which the gas is either in thermal equilibrium or in photoionization equilibrium.

Nebulae, such as, for example, H II regions, have been described with the spherical model of Osterbrock (1974) (e.g. Sankrit & Hester 2000), yet in reality most have a more complex geometry (Pérez et al. 2001; Simpson et al. 2004; McLeod et al. 2016). Morisset (2013) combines spherically symmetric CLOUDY models to account for this more complex geometry. Jin et al. (2022) adopted a fully self-consistent Monte Carlo radiative transfer (MCRT) technique in MAPPINGS-v that can handle such complex geometries. Both models solve for the equilibrium solution and ignore the possible impact of the non-equilibrium effects on emission line diagnostics, and, more importantly, assume that the density structure of the nebula is relatively simple and known a priori.

Nearby star-forming regions have been mapped in detail using integral field spectroscopy (e.g. Rousseau-Nepton et al. 2019; Groves et al. 2023; Drory et al. 2024), revealing filaments of high-density neutral or molecular gas delineating ionized regions of lower density (e.g. McLeod et al. 2021). It is unclear whether the emission lines emitted by these intricate structures can be well described or understood with current relatively simple models of such H II regions. This can be tested by performing more realistic radiation-hydrodynamic simulations of nebular regions and generating mock IFU data cubes from them. Such radiation-hydrodynamical simulations model in detail how a star-forming cloud or the ISM of a galaxy is shaped by radiation, supernovae, winds and jets (see, for example, the SILCC² (Walch et al. 2015) and STARFORGE³ (Grudić et al. 2021) projects). These simulations perform RT for a small set of photon energies with the aim of computing the ionization states of important gas coolants, i.e., typically H I, He I and He II-ionizing photons. The emissivity of this gas in the lines of interest is computed in post-processing (Hirschmann et al. 2017, 2019, 2023b).

Unlike lines such as [O III] $\lambda 5007$ or [N II] $\lambda 6583$, which are excited by collisions, excited states of hydrogen result predominantly from recombinations in a photo-ionised gas, hence they are referred to as hydrogen *recombination* lines. Hydrogen recombination lines are typically amongst the most luminous nebular emission lines and as such have often been the main focus in astrophysical studies. For example, the H α ($n = 3 \rightarrow 2$) line is widely used as an indicator for star formation, since, in photo-ionisation equilibrium, the recombination rate equals the photo-ionisation rate, and the latter is a measure of the rate at which young, massive stars are formed (Kenricut 1998). The emissivity of gas of given density, ionisation state, and temperature in hydrogen recombination lines was calculated in a series of papers in the 1930s (Menzel 1937; Menzel & Baker 1937; Baker & Menzel 1938). These papers showed that recombination, rather than collisional excitation, is the main channel that populates the hydrogen atom's excited states under typical nebular conditions. The excited atom emits a series of hydrogen lines as it cascades to the ground state, making the nebula glow at well-defined wavelengths.

These early papers discussed two limiting cases to describe hydrogen recombination in a nebula. In ‘Case A’, the nebula is optically

thin in the Lyman series lines (transitions to $n = 1$, where n is the usual principal quantum number), whereas in ‘Case B’, the nebula is optically thick in those lines. We note that these are just limiting cases, and in practice, neither approximation is accurate in all situations. Baker & Menzel (1938) argued that Case B is the better approximation for typical nebular conditions. Dipole-allowed transitions need to satisfy the selection rule $\Delta l = \pm 1$, in terms of changes to the angular quantum number l , yet that rule was not taken into account in these papers even though this selection rule had been pointed out already by Bethe et al. (1933). Brocklehurst (1971) revisited the problem, showing that the l -states at given n are generally *not* in statistical equilibrium (i.e. the number density of H I in a given l state is **not** $\propto 2l + 1$), and this affects the emissivities. Tables of recombination line emissivities for a range of gas densities and temperatures were published by Hummer & Storey (1987) and Storey & Hummer (1988, 1995). The lowest density in the table is 10^2 cm^{-3} , which may be insufficient for certain applications. Martin (1988) extended these calculations to lower densities.

Simulations can be post-processed to compute hydrogen recombination line emissivities by interpolating from published tables (e.g. Katz 2022; McClymont et al. 2025), or by constructing tailor-made interpolation tables using, for example, CLOUDY (e.g. Hirschmann et al. 2023a). Alternatively, Raga et al. (2015) suggested computing the emissivities directly, given the temperature and density of the gas, by computing the rate at which levels are populated by recombinations and depopulated by radiative transitions under the assumption that l -states within an n -level are populated according to their statistical weights, which we will show in this paper is not accurate for photo-ionized nebulae. The method of Raga et al. 2015 is widely used in ISM emission line studies. For example, Silva et al. (2018) used it to predict intensity maps and power spectra of H α , Rodríguez-González et al. (2023) used it to calculate H α emission in planetary nebulae. The model was also used to calculate H α emission in post-processing of simulations of AGN outflows (Richings et al. 2021) and simulations of H II regions and the ISM of isolated disc galaxies (Richings et al. 2022).

How consistent are the predicted emissivities between different methods and between different tables? In this paper, we present a method called HyLIGHT for computing hydrogen population levels and hence line emissivities for hydrogen recombination lines directly, given the temperature, density, and ionisation state of the emitting gas. This allows one to predict hydrogen line emissivities for hydrodynamical simulations that include radiative transfer, and enables such simulations to be compared to observations. An advantage of HyLIGHT over using interpolation from a CLOUDY table is that our method uses the ionisation state computed by the simulation directly. This ionisation state may include non-equilibrium effects, which cannot be handled by CLOUDY, which assumes photo-ionisation equilibrium. In addition, HyLIGHT is not restricted to any particular geometry.

The paper is organised as follows. In § 2, we compare predictions for hydrogen line emissivities between different published models, showing that there are significant differences between them. We introduce our own model in § 3. The code is implemented as a publicly available PYTHON package⁴. HyLIGHT directly computes the level population of hydrogen atoms in a gas of a given density and temperature, taking into account radiative recombination and collisional excitation from the ground state. We compare the resulting level population and line emissivities to CLOUDY. As an example application,

² <https://hera.ph1.uni-koeln.de/silcc/>

³ <https://starforge.space/>

⁴ <https://github.com/YuankangLiu/HyLight>

we post-process a radiation-hydrodynamical simulation of an H II region, performed with SPARCS (Chan et al. 2025). We use HyLIGHT to compute level populations and input the result into RADMC-3D (Dullemond et al. 2012), which performs line radiative transfer and outputs a mock IFU data cube.

2 HYDROGEN RECOMBINATION LINES: COMPARISON OF MODEL PREDICTIONS

Consider a hydrogen atom in the $n = 3$ state. When the electron transitions to the $n = 2$ state, an H α photon is emitted. The H α emissivity, $\epsilon_{3,2}$, is set by the level population of the $n = 3$ state,

$$\epsilon_{3,2} = (n_{3s} A_{3s,2p} + n_{3p} A_{3p,2s} + n_{3d} A_{3d,2p}) h\nu_{3,2}, \quad (1)$$

where n_{nl} is the density of hydrogen atoms in state nl , $A_{nl,n'l'}$ is the spontaneous transition rate from the $nl \rightarrow n'l'$ state (the Einstein A coefficient), and $h\nu_{3,2}$ is the photon energy corresponding to the transition; l indicates the angular momentum quantum number, with the usual convention that the $l = 0, 1$ and 2 states are denoted by s, p and d . This equation accounts for the $\Delta l = \pm 1$ selection rule for dipole-allowed transitions but neglects stimulated emissions (e.g. Rybicki & Lightman 1979). The key to computing the emissivities of hydrogen lines is therefore computing the level populations n_{nl} ($A_{nl,n'l'}$ is an integral involving the products of the nl and $n'l'$ electron orbitals). Calculating the n_{nl} is not trivial. Various authors use different approximations, and we begin by quantifying the resulting differences in the predicted emissivity for common recombination lines in two simple setups: (1) a spherical cloud of uniform-density hydrogen gas at constant temperature, with a central ionizing source, and (2) a thin, spherical shell of uniform-density hydrogen gas at constant temperature, with a central ionizing source.

2.1 Idealized test set-ups for model comparisons

We use two simple geometries to contrast different models for calculating hydrogen line emissivities. In both cases, the gas is static, consists of pure hydrogen gas with a density of 100 cm^{-3} , does not contain dust or molecules, and its temperature is kept constant at $T = 10^4 \text{ K}$. The photon source emits ionizing photons at a rate of 10^{48} s^{-1} with a blackbody spectrum of temperature 10^5 K . These values are typical for H II regions (Osterbrock & Ferland 2006). The two example set-ups are as follows:

(i) *Idealised spherical model.* Spherical models of H II regions are widely used historically (see Osterbrock 1974; Pellegrini et al. 2012, for examples). In these models, a central hot star ionizes the surrounding gas, with the ionization front stalling at the Strömgren radius. In our set-up, the inner edge of the gas cloud is positioned 0.01 pc away from the ionizing source. These spherical setups are labelled ‘Sph’ in Table 1, which also lists all the other setups we have used in this paper along with their specific parameters.

(ii) *Idealised shell models.* Shell models are widely used to explore the ionisation and emission properties of gas for a particular set of physical conditions and for a particular incident radiation field, without taking into account the effects of radiative transfer on the incident spectrum (e.g. D’Agostino et al. 2019). In our set-up, the shell of gas is positioned 0.01 pc from the same source as in (i), and the shell is 1 cm thick to keep any radiative transfer effects to a minimum. Such fiducial setups are labelled as ‘Sh’ in Table 1 depending on the method to compute the recombination rate.

We compute the ionization state of the gas in photoionization equilibrium using CLOUDY version C23.01¹ (Ferland et al. 1999, recently described in Ferland et al. 2017; Gunasekera et al. 2023). We extract the electron density, n_e , proton density, n_p , and neutral hydrogen density, n_{HI} , as a function of distance r from the source; these serve as input for calculating the emissivities in all models.

2.2 Atomic models

Given the two types of setups, we compute and compare the level population and hence emissivity in hydrogen recombination lines for several atomic models:

(i) *The CLOUDY model.* CLOUDY calculates the emissivity using a built-in hydrogen model. The level population is computed accounting for collisional excitation and de-excitation (including collisions that change n and those that change l at given n), level-resolved recombinations (*i.e.* accounting for the fact that the recombination rates depend on both n and l), stimulated emission, and absorption of lines from the source and from the nebula. By default, CLOUDY uses 10 l -resolved energy levels, (*i.e.* principal quantum numbers $n = 1 \rightarrow 10$, with $l = 0 \rightarrow n - 1$ for each n). The code accounts for levels $n > 10$ using ‘collapsed’ (not l -resolved) levels, by default using 10 of these². We investigate the convergence of the CLOUDY results when increasing the number of level-resolved levels in § 3.2 and Appendix A, see also Guzmán et al. 2025. Based on our findings, we generate a ‘Reference’ CLOUDY model which employs 100 l -resolved levels and 1 collapsed level. The reference model is labelled ‘Ref’ throughout this paper, see also Table 1.

(ii) *The Storey & Hummer tables.* Storey & Hummer (1995) published interpolation tables of level populations and emissivities as a function of density and temperature of emitting gas for hydrogenic ions. Their model includes an adaptive number of nl -resolved levels and is described in Hummer & Storey 1987; Storey & Hummer 1988 and Storey & Hummer 1995.

(iii) *The Raga et al. model.* Raga et al. (2015) computed the level populations of a 5-level hydrogen atom. The model includes collisional excitations, but recombinations and collisions are not l -resolved. The model assumes that the level population for a given n are proportional to their statistical weights, $2l + 1$.

(iv) *Our model.* The HyLIGHT model, presented in this paper, calculates the level population for a hydrogen atom where the user can select the maximum number of levels used, n_{max} , and accounts for all l -states for levels $n = 1 \rightarrow n_{\text{max}}$. Details of the model are presented in the next section. In this section, we set $n_{\text{max}} = 100$. The model is similar to CLOUDY’s built-in methods but omits certain processes (*e.g.* Lyman pumping, l -mixing collisions, collisional excitation and de-excitation above the ground state). These approximations are good under typical nebular conditions, as we show in § 3.

(v) *The LTE model.* We also compute the level population assuming local thermodynamic equilibrium (LTE) for reference. Details of the LTE calculation are in Appendix C.

The Einstein A coefficients used in HyLIGHT are computed using the code described by Hoang-Binh 1990 and Hoang-Binh 2005. We verified that they are identical to those used in CLOUDY.

¹ <https://gitlab.nublado.org/cloudy/cloudy/-/wikis/home>.

² Recombination to these collapsed levels can be turned off, in which case the total recombination rate coefficient is no longer conserved. This command is referred to as ‘topoff’ in CLOUDY.

Table 1. List of setups used in this paper with the detailed parameters. We vary the properties of the source of ionizing photons (blackbody spectrum or a narrow laser beam), the geometry of the gas (spherical or shell), and whether we specify the nature of recombinations (Case A, Case B, or unspecified). The table also lists the number of l -resolved levels (for $n = 1 \rightarrow n_{\text{resolved}}$ and the number of collapsed levels in the CLOUDY modelling. In all models, the inner radius r_i of all models is kept at 0.01 pc, the hydrogen density is 100 cm^{-3} and the gas temperature is 10^4 K (typical values for H II regions). The ionizing photon rate of the source is $Q(\text{H}) = 10^{48} \text{ s}^{-1}$ to mimic a hot star. For simplicity, only hydrogen is taken into account in these models.

Label	Source spectrum	Cloud geometry	Recombination method	n_{resolved}	$n_{\text{collapsed}}$
Ref - LSph	Laser at 1.1 Ryd	Sphere	Not specified	100	1
Ref - Sph	Blackbody of 10^5 K	Sphere	Not specified	100	1
Ref - ASh	Blackbody of 10^5 K	Shell	Case A	100	1
Def - ASh	Blackbody of 10^5 K	Shell	Case A	10	15
Ref - BSh	Blackbody of 10^5 K	Shell	Case B	100	1
Def - BSh	Blackbody of 10^5 K	Shell	Case B	10	15
Ref - ALSh	Laser at 1.1 Ryd	Shell	Case A	100	1
Def - ALSh	Laser at 1.1 Ryd	Shell	Case A	10	15

2.3 Model comparison

The $\text{H}\alpha$ emissivity, $\epsilon(\text{H}\alpha) \equiv \epsilon_{3,2}$, is compared for the different models and the ‘spherical cloud’ set-up in Fig. 1 (left panel). In all models, $\epsilon_{3,2}$ is nearly constant out to the Strömgren radius, $r \approx 1.5 \text{ pc}$, then drops rapidly. CLOUDY (purple symbols) and the tabulated values from Storey & Hummer (1995) (black diamonds) agree to better than a per cent in the inner parts of the spherical cloud, but start to deviate at larger r . In contrast, the Raga et al. (2015) results (yellow crosses) are 40 per cent lower than CLOUDY in the inner parts of the cloud, but agree to within a few per cent in the outskirts. The level of (dis)agreement between the models is mirrored in the level population of the n_{3s} level (Fig. 1, right panel). Interestingly, here Raga et al. (2015) differs significantly from the CLOUDY values, including in the outer (neutral) parts of the cloud where the emissivity agrees. The reason behind the discrepancy between Raga et al. (2015) and CLOUDY is that the model by Raga et al. (2015) only takes into account atomic levels up to $n = 5$, and l -levels are populated according to their statistical weights, $2l + 1$. The latter assumption is not valid, as we show in detail later. The values obtained from the tables published by Storey & Hummer (1995) differ significantly from the CLOUDY values in the outskirts ($\gtrsim 2 \text{ pc}$). These tables assume that the population level in the ground state is sufficiently low that the collisional excitation rate from the ground state can be neglected (see Hummer & Storey 1987 § 4 and Storey & Hummer 1995 § 2). This is not a good approximation for the parameters in this test, as we show later. In short, where the other models differ from CLOUDY, we have good reason to believe that they are inaccurate.

The red lines in both panels are computed using HyLight, the model presented in this paper. The predictions from HyLight agree to within a few per cent with CLOUDY throughout the cloud, both in terms of emissivity and level population.

Tables 2 & 3 compare some models for the shell set-up for several hydrogen recombination lines, with luminosity scaled to that of the CLOUDY reference model (assuming either Case A or Case B). The first column compares to the reference CLOUDY model ‘Def’, for which we do not specify either Case A or Case B recombination - the differences are of order 10 per cent for the Balmer lines, but reach up to 25 per cent for Brackett α . The LTE values differ by up to an order of magnitude from those predicted by CLOUDY: local thermodynamical equilibrium is clearly a poor approximation. The Storey & Hummer (1995) tabulated values agree with the CLOUDY calculations at the per cent level in the worst case of Brackett α . The Raga et al. (2015) values differ at the 50 per cent level or more. Finally, the values computed using HyLight agree with CLOUDY to better than one per cent for all lines shown.

We refer to the CLOUDY model as the ‘baseline’ model, as it cap-

tures most physical processes. We find that the results from HyLight compare favourably to those of the other models, and reproduce the CLOUDY results very well. Using CLOUDY models directly to post-process radiation-hydrodynamic simulations can be a daunting task: it requires tabulating population levels as a function of density, temperature and ionising spectrum. In addition, the CLOUDY calculation assumes that the gas is in photo-ionisation equilibrium. Therefore, CLOUDY cannot be used to account for any non-equilibrium effects, whereas the simulation may include these (e.g., the simulations performed using SPARCS by Chan et al. (2025) which we analyse below).

HyLight uses level-resolved, temperature-dependent recombination rates and accounts for collisional excitations from the ground state. We show below that these two processes are dominant in setting the level population under typical nebular conditions. Given the ionization state of the gas - as obtained, for example, from a non-equilibrium radiation hydrodynamical simulation - HyLight computes the level population and the emissivity of the gas for all hydrogen lines. The model does not assume either thermal or ionization equilibrium. It only assumes that the rate of populating a specific nl -state equals the rate at which the state is being depopulated - which is an extremely good approximation. We describe the model in more detail next.

3 COMPUTING THE LEVEL POPULATION IN HYDROGEN: THE HyLight MODEL

The ionization state of hydrogen gas in a nebula can be out of equilibrium - meaning the rate at which atoms are ionized differs from the rate at which they recombine. This can result from sudden changes in density or temperature of the gas (for example, due to shocks), or from a sudden increase or decrease in the photo-ionizing flux (for example, because of variability of the source, or due to shadowing). The timescale to reach equilibrium is usually either the photo-ionisation timescale or the recombination timescale.

The level population of neutral hydrogen can also be out of equilibrium. However, the typical timescale to restore equilibrium is of order the inverse of the Einstein A values, and hence very short ($\sim 10^{-6} - 10^{-8} \text{ s}$). In astrophysical scenarios, it is therefore an extremely good approximation to assume that level populations *are* in equilibrium, even when the ionization levels are not.

The equilibrium abundance of a given level is found by equating the rate at which the level is populated to the rate it is depopulated. Levels are populated by (1) direct recombinations, described by a recombination coefficient, (2) spontaneous transitions, described by the Einstein A coefficients, (3) induced transitions, described by the Einstein B coefficients, (4) absorption of photons, and (5) collisions.

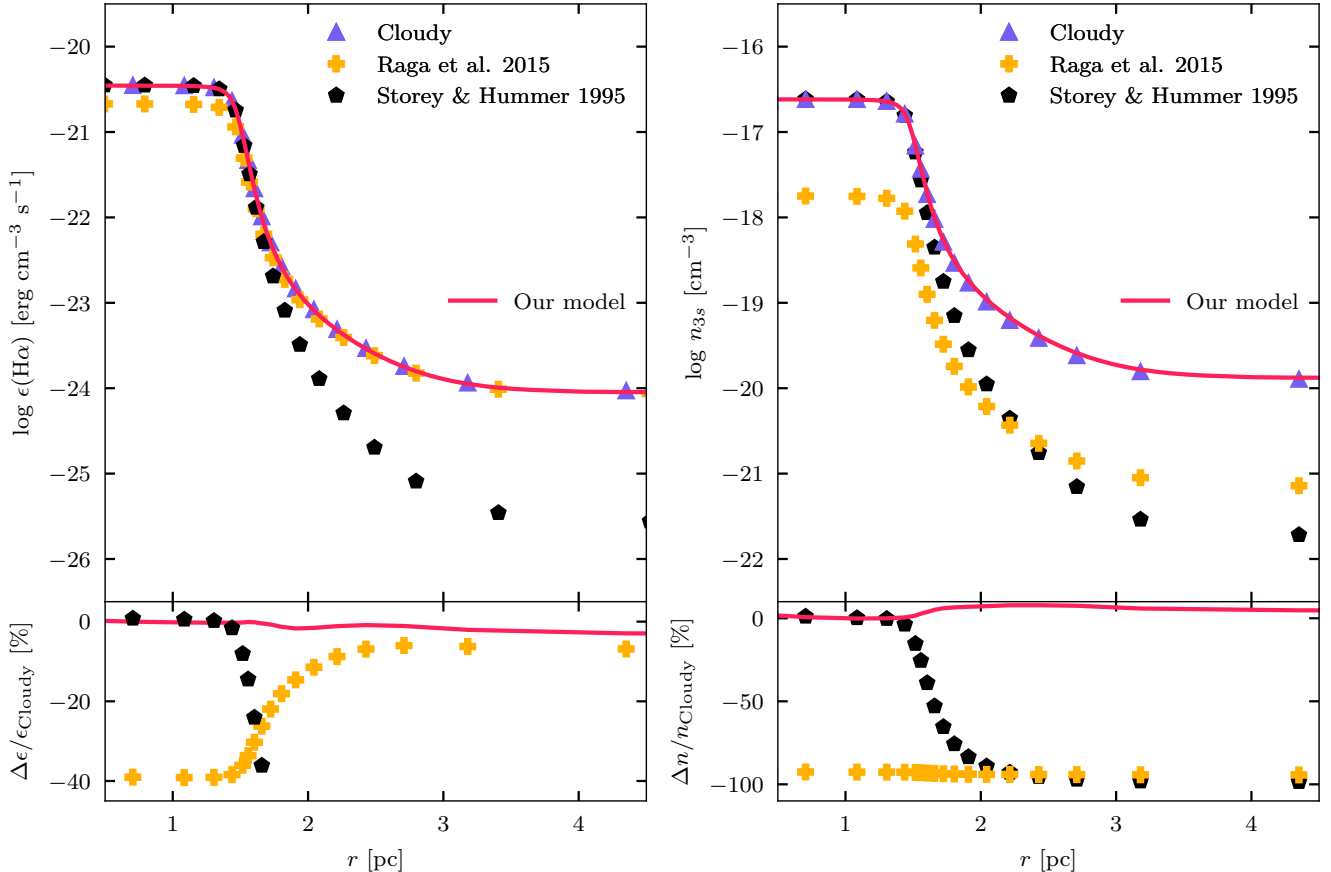


Figure 1. *Left panel:* Profile of $H\alpha$ emissivity, $\epsilon(H\alpha) \equiv \epsilon_{3,2}$, of the idealised spherical setup for different models: the reference CLOUDY model ‘Ref-Sph’ (purple triangles), the Raga et al. (2015) model (yellow crosses) and the tabulated values from Storey & Hummer (1995) (black diamonds). The *top panel* shows the emissivity; the *lower panel* is the relative difference in emissivity compared to ‘Ref-Sph’ in per cent. In all models, the emissivity is approximately constant inside the Strömgren radius, $r \approx 1.5$ pc, then drops rapidly. Different models differ by up to 50 per cent from the CLOUDY prediction. In particular, Storey & Hummer (1995) values at large radii ($\gtrsim 2$ pc) differ by over 40 per cent in terms of emissivity. *Right panel:* Same as left panel, but for the density of hydrogen atoms in the $3s$ state. Different models now differ by up to 100 per cent from the CLOUDY prediction. In all panels, the red line is the prediction from the model described in this paper. Our model agrees with the CLOUDY prediction within 1 per cent in terms of the total $H\alpha$ luminosity.

Table 2. Line luminosities for selected recombination lines predicted by different models for the thin shell set-up; Case A recombination is imposed for all models, and luminosities are relative to the CLOUDY reference model ‘Ref - ASh’.

Luminosity relative to Ref - ASh	Def - ASH	LTE	Storey & Hummer 1995 Case A	Raga et al. 2015 Case A	This work - Case A
Balmer α	0.902	12.424	1.007	0.409	1.001
Balmer β	0.962	7.441	1.005	0.552	1.001
Balmer γ	0.980	5.788	1.004	0.536	0.999
Paschen α	0.825	4.538	1.009	0.337	1.000
Paschen β	0.901	3.763	1.004	0.348	1.001
Brackett α	0.761	2.765	1.013	0.256	1.000

Table 3. Same as Table 2, but now imposing Case B recombination, with luminosities relative to the CLOUDY reference model ‘Ref - BSh’.

Luminosity relative to Ref - BSh	Def - BSh	LTE	Storey & Hummer 1995 Case B	Raga et al. 2015 Case B	This work - Case B
Balmer α	0.977	8.157	1.005	0.608	0.997
Balmer β	1.005	4.956	1.003	0.638	0.997
Balmer γ	1.014	3.907	1.004	0.562	0.998
Paschen α	0.916	4.073	1.009	0.524	0.996
Paschen β	0.967	3.308	1.006	0.476	1.000
Brackett α	0.868	2.631	1.013	0.379	0.993

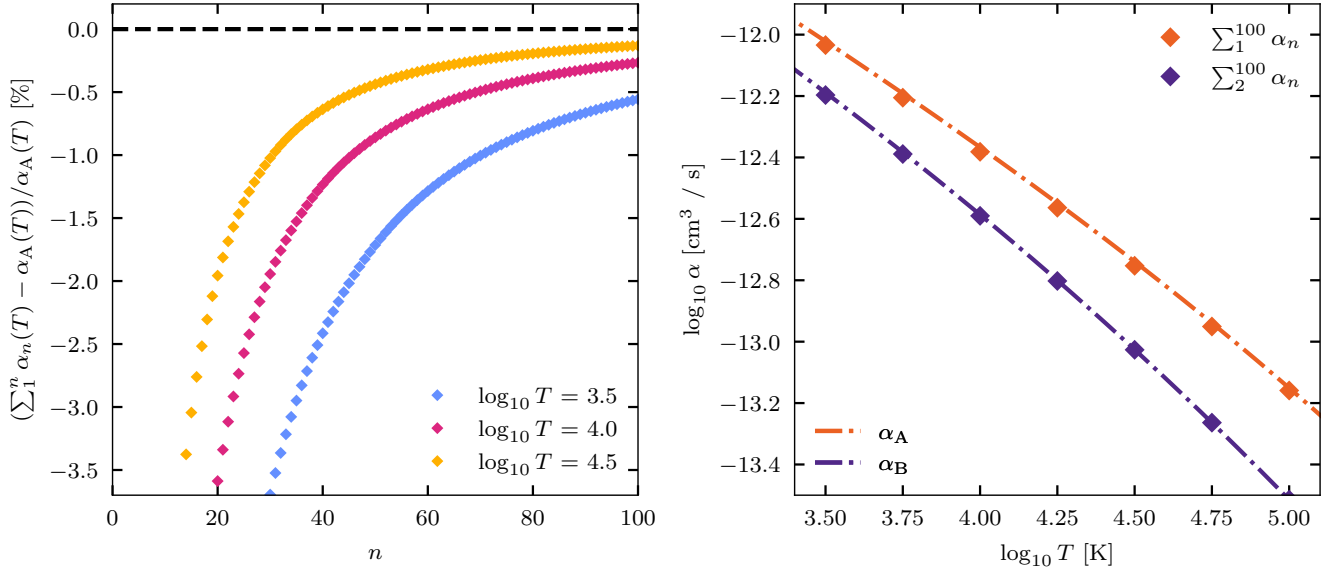


Figure 2. *Left panel:* Cumulative nl -resolved recombination rate, $\sum_{n'=1}^n \sum_{l'=0}^{n'} \alpha_{n'l'}(T)$, up to a given n , for various temperatures as per the legend. Diamonds are the difference in per cent of the cumulative rate compared to the total recombination coefficient, α_A . The black dashed line at 0 is drawn to guide the eye. For $T = 10^4$ K, the cumulative rate for $n = 100$ equals the total rate to better than 0.5 per cent, quantifying the level to which recombinations to levels with $n > 100$ are unimportant in setting the recombination rate. The importance of recombinations to these higher energy levels increases with decreasing T . *Right panel:* Sum of the nl -resolved recombination rates up to and including level $n = 100$ (diamonds) compared to the total recombination rate (lines) for Case A (purple) and Case B (orange). The summed level-resolved recombination rate up to $n = 100$ agrees to better than a per cent with the tabulated values for T in the range $10^{3.5} - 10^{5.5}$ K.

Levels are depopulated by the same processes, except for process (1). The relative importance of these processes depends on the physical properties of the system (density, temperature, ambient radiation field).

We now describe our implementation of a model to compute hydrogen emission lines, called `HyLIGHT` (HYdrogen recombination LIne emission from ionized Gas in varying tHermal condiTions). The code is written in `PYTHON` and publicly available on GitHub¹. Of the processes that set the level population, `HyLIGHT` neglects induced emission and absorption of photons from the source and the nebula (see § 3.5 for the effects of Lyman pumping from source), and further only includes the effects of collisions of hydrogen atoms in the ground state. We will test the impact of the omissions by comparing to `CLOUDY`, which does not make these simplifications. In `HyLIGHT`, the level population is obtained by solving the following set of coupled linear equations,

$$\begin{aligned} & \left[n_p n_e \alpha_{nl}(T) + \sum_{n' > n}^{\infty} \sum_{l'=l\pm 1}^{n'-1} n_{n'l'} A_{n'l',nl} \right] \\ & + \left[n_{\text{HI}} n_e \sum_{n'=n+1}^{\infty} \sum_{l'=0}^{n'-1} q_{1s,n'l'}(T) A_{n'l',nl} \right] = n_{nl} \sum_{n''=1}^{n-1} \sum_{l''=l\pm 1}^{n-1} A_{nl,n''l''}. \end{aligned} \quad (2)$$

Here, n_e , n_p and n_{HI} are the densities of electrons, protons, and neutral hydrogen atoms, $\alpha_{nl}(T)$ is the temperature-dependent level-resolved recombination rate, and $q_{1s,nl}$ is the temperature-dependent collisional excitation rates from the ground state to level nl ; the A 's are the Einstein A coefficients, as before. Note that in general

$A_{n'l',nl} \neq 0$ only if $l' = l'' \pm 1$. The left hand side of Equation (2) is the rate at which level nl is being populated by direct recombinations, and by spontaneous transitions from higher n - the two terms in the first set of square brackets, and by collisions with hydrogen atoms in the ground state - the term in the second set of square brackets. The right-hand side is the rate at which level nl is being depopulated by spontaneous transitions to states with lower n . We will first neglect the collisional term and determine the level population due to radiative transitions only.

3.1 The level population with radiative transitions only

Neglecting collisional processes yields the following equation for the level population,

$$n_p n_e \alpha_{nl}(T) + \sum_{n' > n}^{\infty} \sum_{l'=l\pm 1}^{n'-1} n_{n'l'} A_{n'l',nl} = n_{nl} \sum_{n''=1}^{n-1} \sum_{l''=l\pm 1}^{n-1} A_{nl,n''l''}. \quad (3)$$

Equation (3) can be solved using the ‘Cascade Matrix Formalism’ (henceforth CMF, see e.g. [Seaton 1959](#) and [Osterbrock & Ferland 2006](#)). We start by computing the fraction of spontaneous transitions of a state nl to another state $n'l'$ (with $n' < n$), denoted as $P_{nl,n'l'}$, as

$$P_{nl,n'l'} \equiv \frac{A_{nl,n'l'}}{\sum_{n''=n_{\text{low}}}^{n-1} \sum_{l''=0}^{n'-1} A_{nl,n''l''}}, \quad (4)$$

where $n_{\text{low}} = 1$ in the summation in the denominator (see later for why we introduce this variable). We compute the P 's using the A 's calculated with the code of [Hoang-Binh \(2005\)](#). The numerical values we find are in excellent agreement with those listed in [Bethe et al. 1933](#) (table 19, page 446).

¹ <https://github.com/YuankangLiu/HyLight>

The cascade matrix, $C_{nl,n'l'}$, is defined recursively in terms of the P 's, as

$$C_{nl,n'l'} = \sum_{n''=n+1}^n \sum_{l''=l\pm 1} C_{nl,n''l''} P_{n''l'',n'l'} \quad (5)$$

$$= P_{nl,n'l'} + \sum_{l''=l\pm 1} [C_{nl,n-1l''} P_{n-1l'',n'l'} + C_{nl,n-2l''} P_{n-2l'',n'l'} + \dots], \quad (6)$$

with $C_{nl,n-1l'} = P_{nl,n-1l'}$ and $C_{nl,n'l'} = \delta_{ll'}$ (the Kronecker delta function). The recurrence guarantees that $C_{nl,n'l'}$ is the fraction of spontaneous decays from the state nl that end up in the state $n'l'$, either via a direct spontaneous decay or via a ‘cascade’ of spontaneous decays through intermediate states. As noted before, we need to be satisfied with some maximum value n_{\max} of n that we will account for in the calculation of the C 's to start the recurrence.

We can now use the cascade matrix to compute the rate at which a level is populated, and Equation (3) becomes

$$n_p n_e \sum_{n'=n+1}^{\infty} \sum_{l'=0}^{n'-1} \alpha_{n'l'}(T) C_{n'l',nl} = n_{nl} \sum_{n''=n_{\text{low}}}^{n-1} \sum_{l''=l\pm 1} A_{nl,n''l''}. \quad (7)$$

The left-hand side is the rate at which the state nl is populated, the right-hand side the rate at which it is de-populated, and we can compute the n_{nl} from the C 's, A 's and α 's:

$$n_{nl} = n_p n_e \frac{\sum_{n'=n+1}^{\infty} \sum_{l'=0}^{n'-1} \alpha_{n'l'}(T) C_{n'l',nl}}{\sum_{n''=n_{\text{low}}}^{n-1} \sum_{l''=l\pm 1} A_{nl,n''l''}} \equiv n_p n_e R_{nl}(T). \quad (8)$$

Equation (8) shows that the level population $n_{nl} \propto n_p n_e$, with a proportionality constant, R_{nl} , that depends on temperature. The numerator of R_{nl} is the net rate at which level nl is being populated by recombinations, either directly to state nl , or to a higher energy state which decays to level nl by a series of spontaneous transitions, as described by the cascade matrix C . This term is sometimes called the effective recombination rate coefficient to level nl , $\alpha_{nl}^{\text{eff}}(T)$,

$$R_{nl}(T) = \frac{\alpha_{nl}^{\text{eff}}(T)}{\sum_{n''=n_{\text{low}}}^{n-1} \sum_{l''=0}^{n''-1} A_{nl,n''l''}} \quad (9)$$

$$\alpha_{nl}^{\text{eff}}(T) = \sum_{n'=n+1}^{\infty} \sum_{l'=0}^{n'-1} \alpha_{n'l'}(T) C_{n'l',nl}. \quad (10)$$

• *Evaluating the α_{nl} 's.* When gas is in thermodynamic equilibrium with an ambient blackbody radiation field with temperature T , detailed balance ensures that the photo-ionization rate (from any level) is equal to the corresponding recombination rate (see Rybicki & Lightman 1979 §10.5 and the appendix of Ferland et al. 1992). CLOUDY uses this to compute the level-resolved α_{nl} 's. We extract these rates from CLOUDY outputs. Fig. 2 (left panel) shows the difference in per cent of the sum of resolved recombinations up to some level, n , compared to the total rate, for various temperatures (different colours). At $T = 10^4$ K, recombinations to levels $n > 100$ contribute less than 0.5 per cent to the total rate. Fig. 2 (right panel) compares the result of summing the level-resolved recombination rates up to level $n = 100$ starting from $n = 1$ (α_A or ‘Case A’ recombination) or from $n = 2$ (α_B or ‘Case B’ recombination) against the values tabulated in Ferland et al. (1992): the computed and tabulated rates agree to better than 1 per cent.

• *Evaluating the Einstein A 's.* We evaluate the Einstein A coefficients using a FORTRAN 77 code written by Hoang-Binh (2005)². We verified that the resulting values agree to typically better than 1 per cent with those tabulated in the NIST database³. The FORTRAN code also allows us to compute Einstein A values not in the NIST database.

Once the α 's and Einstein A 's are known, the relation Equation (5) shows how to compute the $C_{nl,n'l'}$, provided the matrix elements are known for all larger n . Applying the recurrence relation therefore requires choosing a highest population level, $n = n_{\max}$, that we will account for, and setting $C = P$ for that highest level (ie truncating the cascade to transitions below n_{\max}). We can understand intuitively that the level population will converge with increasing n_{\max} , simply because the recombination rate α_{nl} decreases with increasing n . The right panel of Fig. 2 shows this convergence: the sum of the level-resolved α_{nl} 's up to $n = 100$ differs from the total α_A by less than 1 per cent for all temperatures above $10^{3.5}$ K. By default, we start the recurrence from $n_{\max} = 100$, meaning that we neglect recombinations to levels $n > 100$. Below, we investigate in more detail the extent to which this approximation affects our results.

In summary, we compute the values of the Einstein coefficients following Hoang-Binh 2005, and use them to compute the cascade matrix, C . We then extract level-resolved recombination rates, α_{nl} , from CLOUDY. Both C and α_{nl} are restricted to $n \leq n_{\max}$, specified by the user. We can then compute the level population from Equation (8), for any $n \leq n_{\max}$, for gas at a given temperature, T , with a given level of ionization specified by the electron and proton density, n_e and n_p .

The left-hand side of Equation (7) is reminiscent of the left-hand side in the equation for the neutral fraction, x , of gas with hydrogen density n_H in photoionization equilibrium,

$$n_{\text{HII}} n_e \sum_{n=n_{\text{low}}}^{\infty} \alpha_{nl}(T) = x n_H \Gamma, \quad (11)$$

where Γ is the photoionization rate. We exploit the similarity between these two equations to gain physical insight, as follows. Write the solution for the neutral fraction x from Equation (11) in the form

$$x \equiv \frac{n_{\text{HI}}}{n_H} = (1-x)^2 \frac{\tau_i}{\tau_r}, \quad (12)$$

where τ_r is the recombination time and τ_i the ionization time,

$$\frac{1}{\tau_r} = n_H \sum_{n=n_{\text{low}}}^{\infty} \sum_{l=0}^{n-1} \alpha_{nl}(T) \equiv \alpha_r(T); \quad \frac{1}{\tau_i} = \Gamma. \quad (13)$$

When elements other than Hydrogen are neglected, $n_e = n_{\text{HII}} = (1-x)n_H$. Next we re-write Equation (7) in the form

$$x_{nl} \equiv \frac{n_{nl}}{(2l+1)n_H} = (1-x)^2 \frac{\tau_{A, nl}}{\tau_{nl}}, \quad (14)$$

where we defined

$$\frac{1}{\tau_{nl}} = \frac{n_H}{2l+1} \sum_{n'=n+1}^{\infty} \sum_{l'=0}^{n'-1} \alpha_{n'l'}(T) n C_{n'l',nl} \quad (15)$$

$$\frac{1}{\tau_{A, nl}} = \sum_{n''=n_{\text{low}}}^{n-1} \sum_{l''=l\pm 1} A_{nl,n''l''}.$$

Comparing Equations (12) and (14) brings out the similarity between the two cases: when $x \ll 1$, the neutral fraction is set by the ratio τ_i/τ_r , where τ_i is the rate at which neutral gas is being depleted due to photo-ionization, and τ_r the rate at which it is formed due

² The code is available at <https://data.mendeley.com/datasets/3drgznwty8/1>.

³ NIST Atomic Spectra Database Lines Data for Atomic Hydrogen.

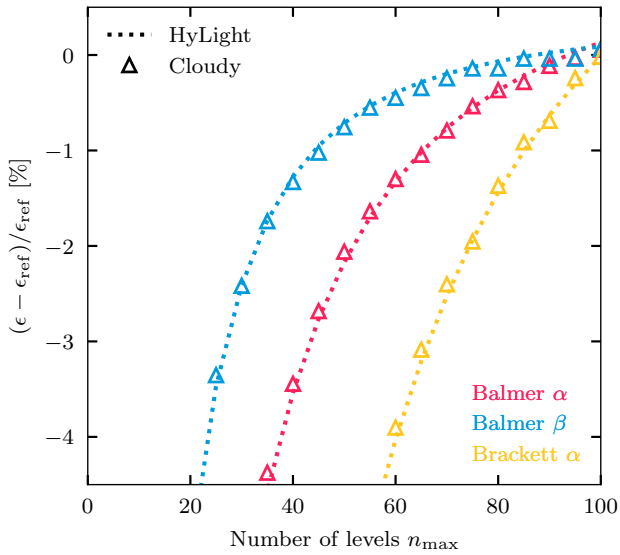


Figure 3. Convergence of the emissivity, ϵ , for selected hydrogen transitions for different models in Case A. The reference setup is ‘Ref - ALSh’ as shown in Table 1. The horizontal axis is the number of resolved levels in the atomic model, while the vertical axis indicates the emissivity difference in per cent between a given model and the reference model. The dotted line shows the predictions from radiative-only HyLIGHT predictions. The open triangles are predictions from the ‘LShA - Ref - RR’ CLOUDY model, which only includes radiative processes, as described in Table 4. There is excellent agreement between CLOUDY and HyLIGHT. As the number of levels increases, both models converge to the reference model. We conclude that 100 resolved levels is sufficient to produce accurate line emissivities.

to recombinations. Similarly, for $x \ll 1$, the fraction of the gas in a given level, x_{nl} , is the ratio $\tau_{A,nl}/\tau_{nl}$, where $\tau_{A,nl}$ is the rate at which the state nl is depopulated due to spontaneous decay, and τ_{nl} is the rate at which it is populated due to the cascade from higher levels.

We can combine Eqs. (12) and (14) to obtain a relation between the fraction of hydrogen atoms in a given state, the neutral fraction, and ratio’s of characteristic times, valid when $x \ll 1$,

$$x_{nl} = x \frac{\tau_r}{\tau_{nl}} \frac{\tau_{A,nl}}{\tau_i}. \quad (16)$$

We note that τ_r and τ_{nl} are both proportional to $1/n_H$, so that their ratio is density independent; since τ_i and $\tau_{A,nl}$ also do not depend on n_H , x_{nl}/x is density independent as well. Interestingly, the ratio x_{nl}/x also depends only relatively weakly on temperature.

3.2 Convergence of the level population with n_{\max}

The recurrence calculation used to evaluate the cascade matrix C using Equation (5) requires choosing a maximum n level, n_{\max} , that is accounted for in the calculation. Here, we investigate the convergence of the results when increasing n_{\max} .

The set-up is that of a thin shell with a source in the centre. Recombinations are forced to be in the Case A limit. Rather than using a blackbody spectrum for the ionizing source as we did so far, we instead use a source which emits ionizing photons in a very narrow⁴ energy range around 1.1 Ryd (termed ‘laser’ in CLOUDY;

the photon luminosity is $Q(H) = 10^{48} \text{ s}^{-1}$). Such a sharply peaked spectrum avoids that hydrogen atoms in the ground state are excited by absorbing high-order Lyman photons from the source (a process not accounted for in our model). We investigate the importance of such ‘Lyman pumping’ in § 3.5. The model is labelled as ‘Ref - LShA’ model in Table 1.

We use CLOUDY to compute the ionization state of the gas in the shell. We then compute the emissivity for a series of hydrogen lines (i) using CLOUDY which includes collisional effects by default, (ii) using CLOUDY but restricting its calculation to include radiative transitions only, and (iii) the radiative-only HyLIGHT model, which is restricted to radiative transitions. For all three cases, we compute the emissivity while varying the number of levels (the number of l -resolved in CLOUDY, n_{res} , and the maximum number of levels included in our cascade matrix calculation, n_{\max}). The model (i) is labelled ‘Ref - ALSh’ and the model (ii) is labelled ‘Ref - ALSh - RR’ in Table 4. The table shows in detail which physical processes are enabled or disabled. We compare the results of models (ii) and (iii) to that of model (i) in Fig. 3. Different colours correspond to Balmer α (red), Balmer β (blue) and Brackett α (yellow). The CLOUDY model with radiative processes only is shown by open triangles; our HyLIGHT model is shown by dotted lines. All emissivities are scaled to the prediction by the model (i), denoted by ϵ_{ref} in Fig. 3, which has all the physical processes enabled and an atomic model of 100 resolved levels and one collapsed level. Our radiative-only HyLIGHT model and the radiative-only version of CLOUDY agree very well for all n , both converging to better than a per cent to ϵ_{ref} when $n_{\text{res}} \geq 80$. The Brackett emissivity converges more slowly than the Balmer emissivities. The comparison between the model (i) (Ref - ALSh in Table 4) and the model(ii) (Ref - ALSh - RR in Table 4) is detailed in Appendix A.

We conclude from the above comparison that we need values of at least $n_{\max} \sim 100$ in our model (and of n_{res} in CLOUDY) to obtain converged results in the computation of Balmer and Brackett lines. The value of this maximum level may be temperature dependent, and likely needs to be higher for the Paschen and even higher for the Brackett series. We note that the default value in CLOUDY is $n_{\text{res}} = 10$, which may not be high enough to get accurate results for H II-like nebulae. More details on convergence are presented in Appendix A. Interested readers can also refer to Guzmán et al. 2025 for more in-depth discussions. Increasing n_{res} increases the run-time and memory requirements of CLOUDY significantly, but has little impact on the compute time in HyLIGHT.

We further test our choice of n_{\max} in the following more realistic setting. A spherical cloud (hydrogen only, density $n_H = 10^2 \text{ cm}^{-3}$, constant temperature $T = 10^4 \text{ K}$) is ionised by the same laser-like central source as before. We compare our model for recombinations in the Case A and Case B limit (both with $n_{\max} = 100$) to CLOUDY (including collisions, not specifying either Case A or Case B, ignoring Lyman pumping from the source, and setting $n_{\text{res}} = 100$ with one unresolved level). This setup is labelled as ‘Ref - LSph’ in Table 1.

The results are shown in Fig. 4, with CLOUDY results shown by filled blue triangles and HyLIGHT shown with lines (red for Case B, yellow for Case A); the left panel shows the highly-ionised part of the nebula, up to the Strömgren radius at $r \approx 1.5 \text{ pc}$. The left panel shows that our Case B result agrees well with CLOUDY for $r \geq 0.4 \text{ pc}$. However, close to the source, $r \leq 0.1 \text{ pc}$, the optical depth in Lyman lines is small and CLOUDY’s result is closer to our Case A emissivity. Re-

⁴ The relative laser width is chosen to be 0.001. The detailed definition of

relative laser width can be found in CLOUDY documentation. The choice of laser width is discussed in Appendix E.

Table 4. A model variant to the Ref - ALSH model in Table 1). In Ref - ALSH - RR, we disable all collisional processes, including collisional ionisation, collisional excitation and l -mixing.

Models	Collisional ionisation	Collisional excitation	l -mixing	Recombination top-off
Ref - ALSH	On	On	On	On
Ref - ALSH - RR	Off	Off	Off	Off

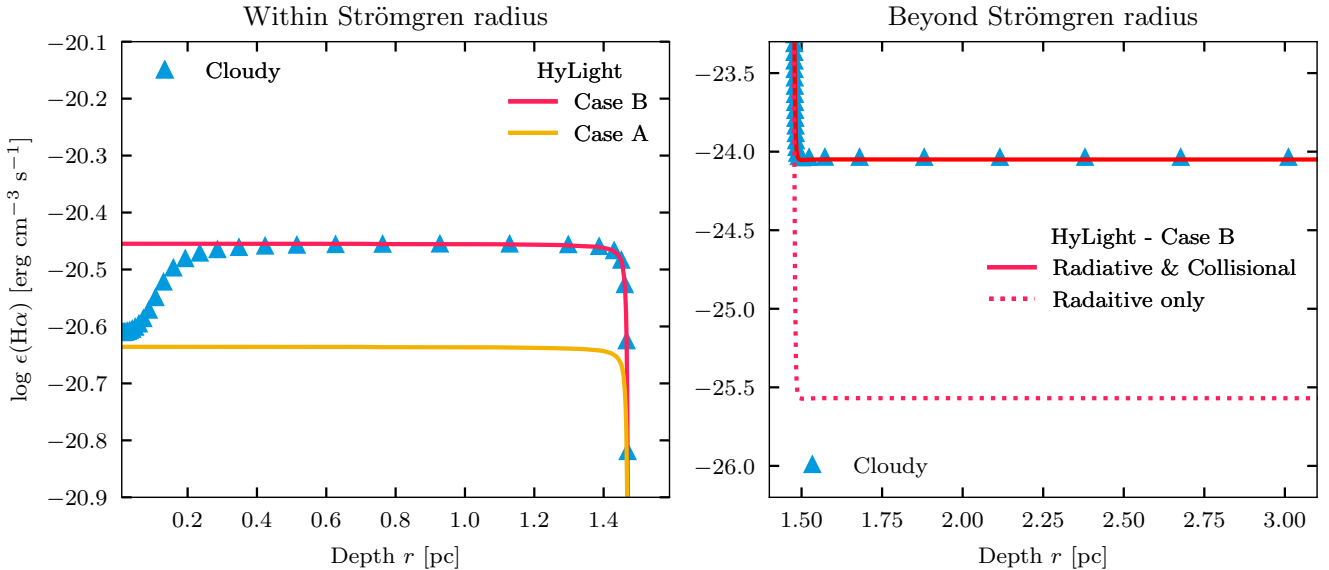


Figure 4. Profile of $H\alpha$ emissivity, $\epsilon(H\alpha) \equiv \epsilon_{3,2}$, of a gas cloud ionized by a laser beam. This CLOUDY setup is labelled as ‘Ref - LSph’ in Table 1. The Strömgren radius is approximately 1.5 pc. The solid curves are HyLIGHT predictions when including radiative *and* collisional contributions. Within the Strömgren radius, the $H\alpha$ emissivity gradually switches from Case A to Case B in the region $r \lesssim 0.4$ pc, a result of the finite optical depth of Lyman photons. Beyond the Strömgren radius, the radiative-only approximation does not hold any more, since collisional excitation of the ground state atoms contributes dominantly: these are not included in the radiative-only calculation. The full HyLIGHT model agrees well with CLOUDY.

producing the resulting dip in emissivity close to the source requires performing radiative transfer of Lyman photons, which we don’t do. The right panel shows the emissivity outside of the Strömgren radius where the gas is mostly neutral. Our calculation using radiative rates only (dotted red line labelled ‘radiative only’) yields an emissivity that is ≈ 1.5 dex below that of CLOUDY. Since the ionising flux is very low, $H\alpha$ emission is a consequence of collisional excitations, which are not included in the radiative-only calculation. The solid red line is our model with collisional excitation included, and this reproduces the CLOUDY results well. We describe these collisional excitation terms next (§ 3.3).

3.3 The level population including collisional excitation

The level population when including collisions from the ground state, as well as radiative transitions, is

$$n_{nl} = R_{nl}(T)n_e n_p + Q_{nl}(T)n_{\text{HI}}n_e$$

$$Q_{nl}(T) \equiv \frac{\sum_{n'=n+1}^{\infty} \sum_{l'=0}^{n'-1} q_{1s,n'l'}(T)C_{n'l',nl}}{\sum_{n''=n_{\text{low}}}^{n-1} \sum_{l''=0}^{n''-1} A_{nl,n''l''}}, \quad (17)$$

where $R_{nl}(T)$ is defined in Equation (10). The level population is therefore a sum of a term due to radiative recombinations (first term) and a term due to collision excitations from the ground state (second term), including both excitations directly to the level nl and

excitations to higher levels that then cascade down to nl . This equation neglects excitations and de-excitation from states other than the ground state, and further makes the approximation that the vast majority of the neutral hydrogen atoms are in the ground state, so that $n_{1s} \approx n_{\text{HI}}$ ⁵.

From Equation (17), we show that the emissivity of a given hydrogen recombination line is also a sum of two terms, one due to recombinations, and one due to collisional excitations,

$$\epsilon_{n'n}(T) = \epsilon_{n'n}^R(T) + \epsilon_{n'n}^Q(T)$$

$$\epsilon_{n'n}^R(T) = n_e n_p h \nu_{n'n} \sum_{l'=\pm l} R_{n'l'}(T) A_{n'l',nl}$$

$$\epsilon_{n'n}^Q(T) = n_e n_{\text{HI}} h \nu_{n'n} \sum_{l'=\pm l} Q_{n'l'}(T) A_{n'l',nl}, \quad (18)$$

where $h \nu_{n'n}$ is the energy of the photon emitted in a transition $n' \rightarrow n$.

We calculate the temperature-dependent $q_{1s,nl}$ rates based on Anderson et al. 2000, Anderson et al. 2002 and Lebedev & Beigman 1998 (see Appendix D for details). Summing these as per Equation (17) yields the collisional terms, $Q_{nl}(T)$.

Similar to the case of the radiative calculations, we need to choose

⁵ As an example, in the set-up ‘Ref - Sph’, at 0.01 pc, the $3s$ level population density is of the order of 10^{-17} cm^{-3} , whereas the ground state $1s$ level population density is $\approx 10^{-5} \text{ cm}^{-3}$, meaning the vast majority of the hydrogen atoms are indeed in the ground state.

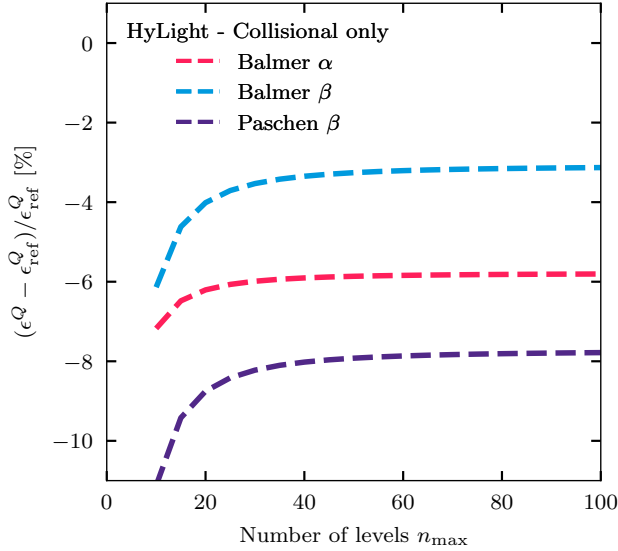


Figure 5. Convergence of the collisional contribution to H α emissivity as a function of the number of resolved levels, n_{\max} . The reference setup is ‘Ref - LSpH’ where the temperature is kept at 10^4 K throughout the cloud. The reference emissivity, ϵ_{ref} , is extracted at 2 pc from the source, where the gas is neutral and collisional excitation dominates over radiative recombination. As the number of levels increases in the model, the line emissivity converges. The difference between the converged answer and the CLOUDY predictions is lower for low-order series (e.g., smaller than 6% for H α and H β) but higher for higher series such as Paschen β (about 8%). Given that the collisional contribution to recombination lines is only relevant in the partially neutral plasma and several orders of magnitude lower than that from radiative recombination within the Strömgren radius, the difference of a few per cent is satisfactory. The differences come from disregard of collisional excitation and de-excitation between and from levels other than the ground state, as well as the exact calculation of collisional excitation rate for nl -resolved levels (see Appendix D).

a maximum value, n_{\max} , for the hydrogen principal quantum number that will be included in the rate calculations (see Equation (17)). We examine the convergence with n_{\max} for some hydrogen lines in Fig. 5. The model simulated is ‘Ref - LSpH’ from Table 1, and we evaluate the emissivity at 2 pc from the source, where the gas is mostly neutral and collisional excitation dominates the emissivity.

The results of our calculations are compared to a CLOUDY reference model which uses $n_{\text{res}} = 100$ resolved levels. We find that our rates converge for $n_{\max} \geq 40$, but the converged value differs from the CLOUDY value by up to 8 per cent for the Paschen β line. This difference is due to collisional excitation and de-excitation from levels other than the ground state, which are accounted for in CLOUDY but not in HyLIGHT. Furthermore, our treatment of converting n -resolved collisional excitation rate to nl -resolved rate is slightly different from CLOUDY (see Appendix D).

We conclude from this comparison that HyLIGHT is not as accurate as CLOUDY in predicting the emissivity of mostly neutral gas - where the emission is dominated by collisional excitation. Fortunately, the emission in nebular regions is very much dominated by the *ionised* component, for which the agreement with CLOUDY is excellent.

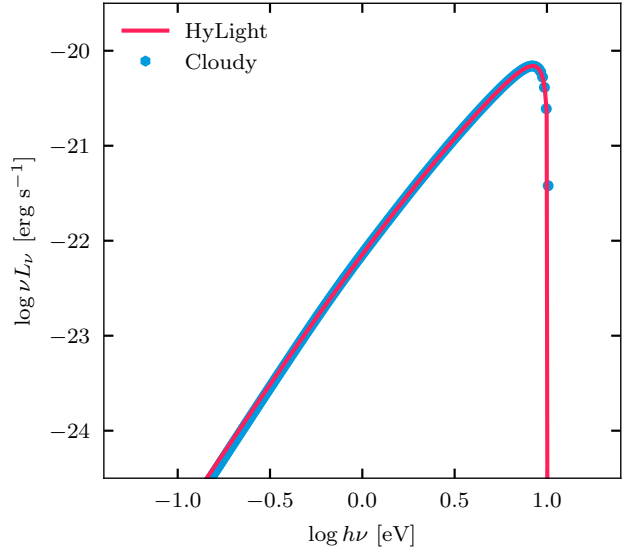


Figure 6. Spectrum of two-photon continuum for the set-up of the model ‘Ref - ASh’ of Table 1 (thin shell ionized by a blackbody). We find the agreement of total luminosity to be better than 0.05 per cent between the model of Equation (21) and that of the reference CLOUDY model.

3.4 Modelling two-photon emission

The $2s \rightarrow 1s$ transition in H 1 is dipole forbidden because it violates the $\Delta l = \pm 1$ selection rule. As a result, the $2s$ state is metastable, with no allowed transition to the ground state. However, an H 1 atom in the $2s$ state can still decay to $1s$ via a virtual intermediate state at a higher order in perturbation theory, a process that results in the emission of two photons. Energy conservation requires that the sum of the photon energies equals that of a Lyman α photon, $h\nu_1 + h\nu_2 = (3/4)$ Ryd. In fact, two-photon transitions are currently the most accurate way to measure the value of the Rydberg constant in eV (e.g. Grinin et al. 2020).

Nussbaumer & Schmutz (1984) (see also Bottorff et al. 2006 and references therein) approximate the rate and spectrum of the $2s \rightarrow 1s$ two-photon transition as

$$A(y) = C \left(y(1-y) [1-D] + \alpha [y(1-y)]^\beta D \right) \\ D = (4y(1-y))^\gamma, \quad (19)$$

with fitting parameters $C = 202.0 \text{ s}^{-1}$, $\gamma = 0.8$, $\alpha = 0.88$, $\beta = 1.53$. The variable $y = \nu/\nu_{2,1}$, where ν is the frequency of one of the two photons (and hence $0 \leq y \leq 1$), and $\nu_{2,1}$ is the frequency of a Lyman α photon. The total rate - *ie* the effective Einstein coefficient due to two-photon decay - is found by integrating over all y ,

$$A_{2s,1s}^{\text{eff}} = \frac{1}{2} \int_0^1 A(y) dy = 8.224 \text{ s}^{-1}, \quad (20)$$

(where the factor 1/2 corrects for double counting), which is close to the value 8.234 s^{-1} quoted by Labzowsky et al. (2006). The calculation above does not account for the presence of an ambient radiation field (see the induced rate calculation in e.g. Bottorff et al. 2006; Chluba & Sunyaev 2006).

The $2p \rightarrow 1s$ transition is dipole allowed. There is also a two-photon decay channel for this transition, but the corresponding rate is much lower than for the $2s \rightarrow 1s$ transition (Labzowsky et al. 2006).

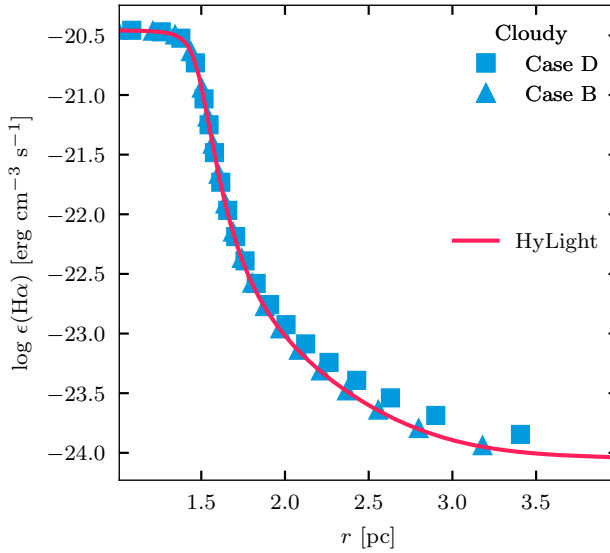


Figure 7. Test of the importance of Lyman photons from the source: H α emissivity profile of a spherical gas cloud ionized by a source with a blackbody spectrum. The model is referred to as ‘Ref - Sph’ in Table 1. The CLOUDY Case B model (triangles) does not account for Lyman photons from the source, whereas the case D model (squares) does. Lyman photons from the source affect the H α emissivity by a few per cent outside the Strömgren radius, $r \approx 1.5$ pc. The HyLight emissivity (red line) does not account for Lyman photons from the source, and agrees well with the CLOUDY case B prediction.

For this reason, we suspect two-photon decay from 2p to 1s is not important in astrophysical situations.

The specific emissivity per unit volume of the 2s to 1s two-photon process, ϵ_ν , is given in terms of the function $A(y)$, by

$$\epsilon_\nu d\nu = h\nu A\left(\frac{\nu}{\nu_{2,1}}\right) n_{2s} \frac{d\nu}{\nu_{2,1}}, \quad (21)$$

where ν is the frequency of the photon emitted in the two-photon process and n_{2s} is the population density of the 2s level.

We compare the specific emissivity computed from Equation (21) for model ‘Ref - ASh’ of Table 1 against the reference CLOUDY model in Fig. 6. The agreement is excellent.

3.5 Processes not included in HyLight

We briefly discuss the physical processes not included in HyLight.

(i) *Line pumping.* Recombining hydrogen gas emits Lyman lines at a rate that can be computed as described in the previous sections. The optical depth to these lines is large in typical H II regions, in particular for the first few Lyman lines. The central optical depth for Lyman α is

$$\tau_c = N_{\text{HI}} \left(\frac{3\pi\sigma_T}{8} \right)^{1/2} f_{1,2} \lambda_{1,2} c \left(\pi b^2 \right)^{-1/2} \approx 1.0 \left(\frac{N_{\text{HI}}}{2.64 \times 10^{13} \text{ cm}^{-2}} \right) \left(\frac{20 \text{ km s}^{-1}}{b} \right), \quad (22)$$

where σ_T is the Thomson cross section, $f_{1,2} = 0.4164$ is the oscillator strength, $\lambda_{1,2} = 1215.67$ Å is the laboratory wavelength, and b is the line width. This equation yields values of τ_c of several thousand for a typical H II region (say $n_{\text{H}} = 10^2 \text{ cm}^{-3}$, extent $r = 3$ pc, and

H I neutral fraction 10^{-4}). For this reason, Case B recombination is usually the better choice. The reasonable agreement between CLOUDY (which includes line pumping) and the Case B HyLight calculation (which does not) of the emissivity - shows that the non-inclusion of line pumping is a reasonable approximation for H II regions.

Nebular gas may also absorb Lyman photons emitted by the *source*, sometimes referred to as Case D. We investigate the impact of this process on the H α emissivity in Fig. 7 for model ‘Ref - Sph’ from Table 1 (spherical cloud, uniform density and temperature, blackbody source). We compare CLOUDY runs for Case B and Case D to the full HyLight model. Within the Strömgren radius, $r_S \approx 1.5$ pc, the two CLOUDY runs and the HyLight model agree very well. Outside r_S , HyLight agrees very well with the CLOUDY Case B run, whereas the CLOUDY Case D emissivity is a few per cent higher. We conclude that in this type of setup, line pumping by photons from the source is not very important. For more discussion on this topic, see e.g. Luridiana et al. 2009. In addition, we intend to use HyLight as a tool for post-processing hydrodynamic simulations; hence, it would be challenging to capture Lyman pumping, which would require us to follow the radiative transfer of Lyman photons.

(ii) *Stimulated emission.* HyLight does not include stimulated emission, whereas CLOUDY does by default. Again, the fact that the Case B HyLight emissivity agrees well with CLOUDY in Fig. 7 implies that stimulated emission is not important in H II regions. Similarly, in terms of post-processing radiation hydrodynamic simulation, it would be challenging to include stimulated emission as it would require coupling the computation of the level populations to the radiative transfer of photons from all sources in the simulation.

(iii) *Collisional processes.* HyLight includes the impact of collisions with electrons on the level population when they excite H I atoms that are in the ground state (1s). However, HyLight neglects collisional excitation from states with $n > 1$ and, in particular, of collisions that change l without changing n . In this case, the l -levels are solutions of Equation (2). We have demonstrated that this limitation only leads to a few per cent difference compared to the full collisional modelling in § 3.3.

The model of Raga et al. (2015) assumes⁶ that l -levels are populated according to their statistical weight, i.e. $n_{nl} \propto (2l + 1)$ at given n . Fig. 8 shows the level populations scaled by $2l + 1$ for the 3s, 3p and 3d states for different models, using the setup ‘Ref - ASh’. The level population is also scaled by n_e , n_p , and F , where F is the average population density for a given n -level:

$$F = \frac{1}{n} \frac{\sum_{n'=n+1}^{\infty} \sum_{l'=0}^{n'-1} \alpha_{n'l'}(T) C_{n'l',nl}}{\sum_{n''=n_{\text{low}}}^{n-1} \sum_{l''=0}^{n''-1} A_{nl,n'l'}} \quad (23)$$

The values in the Raga et al. (2015) model (filled black circles) are then independent of l by construction. The values obtained with CLOUDY (yellow diamonds), Storey & Hummer (1995) (blue crosses) and HyLight (red stars) agree very well with each other, and show that the population of the 3s state is much higher than it would be under the assumption that l -levels are populated according to $2l + 1$ statistical weights. In conclusion, the model of Raga et al. (2015) are not intended to be used for low-density nebular regions but dense planetary nebulae where the gas density is high enough to populate the l -levels within an n -level according to $2l + 1$ statistical weights.

Collisions with protons can change l for a given n (e.g. Pengelly &

⁶ This is not the only difference, for example that model also uses $n_{\text{max}} = 5$ energy levels.

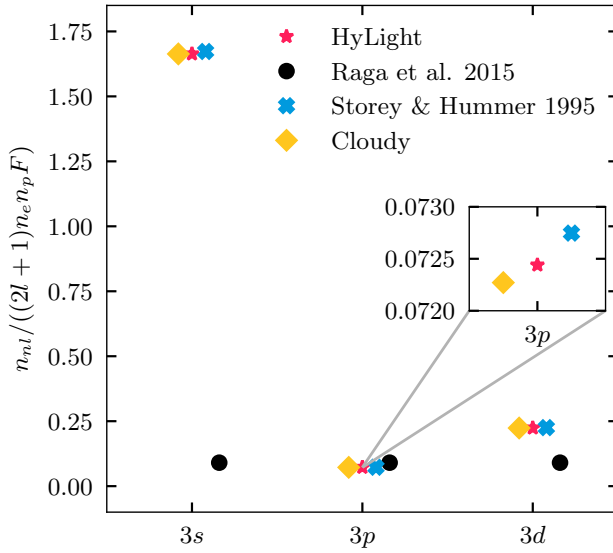


Figure 8. Scaled level population for level n_{3l} as a function of l in set-up Ref-ASh, the factor F is the mean level population calculated using Equation (23). Results are shown for HyLight (red stars), Raga et al. (2015) (black circles), Storey & Hummer (1988) (blue crosses) and Cloudy (yellow diamonds). All models agree well, except for that of Raga et al. (2015) which assumes that the population level is set by statistical equilibrium, $n_{3l} \propto (2l + 1)$. The inset visualizes the good level of agreement. Symbols are slightly offset in the horizontal direction to avoid overlap.

Seaton 1964b; Vrinceanu & Flannery 2001), often referred to as l -mixing. Such collisions do indeed tend to populate l -levels according to their statistical weights. The rate of l -mixing depends on the gas metallicity, temperature, and element abundances, and is strongly dependent on density (Pengelly & Seaton 1964b). By comparing the characteristic l -mixing timescale to the radiative timescale using the method by Vrinceanu et al. (2019), we can estimate the effect of l -mixing on each n -level. At the typical condition for H II regions, for highly excited states, the l -mixing timescale is much shorter than the radiative timescale, hence the l -states tend to be in statistical equilibrium. For lower levels, the time it takes to redistribute the l -states is much larger than that for the radiative process. Therefore, within a given n -level, the l -states will not follow the statistical weight and are simply set by Equation (2). Given the strong density dependence, the impact of collisions is typically formulated in terms of a critical density below which collisions can be safely ignored, with the value of this critical density depending on n .

We illustrate the density dependence of the departure from LTE for three example states ($3s$, $10s$, $66s$) in Fig. 9. Using the setup of ‘Ref-ASh’ in Table 1, we compute the level population with the reference CLOUDY code and compare to the level population values assuming LTE (see Equation (C3) in Appendix C). At the lowest density of $n_H = 10^2 \text{ cm}^{-3}$, all three states are far from LTE, whereas at high density, $n_H = 10^{15} \text{ cm}^{-3}$, they are all in statistical equilibrium. The critical density - the value where the level transitions to statistical equilibrium - is $n_H \approx 10^3 \text{ cm}^{-3}$ for level $66s$, but $n_H \approx 10^{10} \text{ cm}^{-3}$ for $3s$.

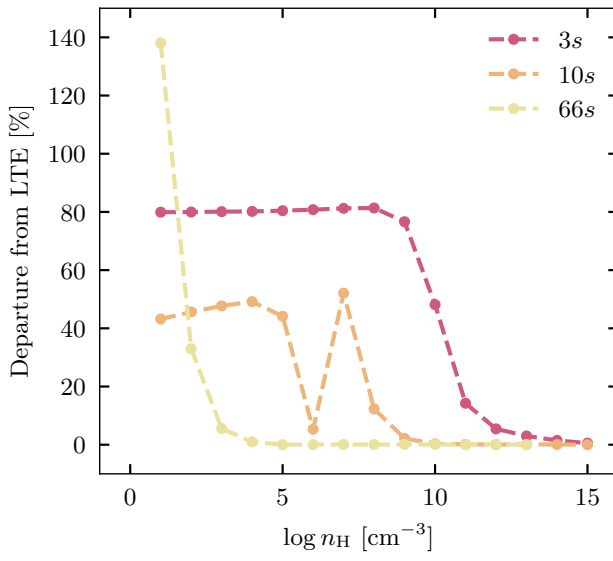


Figure 9. Departure from LTE for different states ($3s$ in red, $10s$ in orange, and $66s$ in yellow) at a fixed temperature of 10^4 K as a function of gas density. The level populations are extracted from CLOUDY ‘Ref - ASh’ setup. The vertical axis shows the deviation from LTE (see Equation C3) in per cent. Lower levels are far from the LTE predictions at low densities. As the gas density increases, all the levels approach equilibrium eventually.

4 EXAMPLE APPLICATIONS OF THE HyLight MODEL

We illustrate the usefulness of the HyLight model with some examples. The first example shows how HyLight branching ratios can be used to relate the emissivity in hydrogen lines to each other or to the ionisation rate. The second example uses HyLight to compute IFU data from a 3-dimensional radiation hydrodynamical simulation.

4.1 Branching ratios and hydrogen line luminosities

We mean by ‘branching ratio’, $B_{nl,n'l'}$ of a particular transition¹, $nl \rightarrow n'l'$, the ratio of the rate at which this transition occurs over the total recombination rate. We similarly define the total branching ratio, $B_{n,n'}$, as the branching ratio for transitions from $n \rightarrow n'$ - summed over all l . As an example, the total branching ratio for the H α transition is

$$B_{3,2}(T) = \frac{dn_{3 \rightarrow 2}(T)}{dt} \frac{1}{n_e n_p \alpha_{\text{tot}}(T)} = \frac{A_{3s,2p} n_{3s}(T) + A_{3p,2s} n_{3p}(T) + A_{3d,2p} n_{3d}(T)}{n_e n_p \alpha_{\text{tot}}(T)}, \quad (24)$$

where $\alpha_{\text{tot}}(T)$ is the total recombination coefficient (which we can choose to be in the Case A or Case B approximation).

We can compute the branching ratio starting from Equation (17) for the level population, so that in general

$$B_{nl,n'l'}(T) = A_{nl,n'l'} \frac{R_{nl}(T)}{\alpha_{\text{tot}}(T)} + A_{nl,n'l'} \frac{Q_{nl}(T) n_{\text{HI}}}{n_p \alpha_{\text{tot}}(T)} \equiv B_{nl,n'l'}^R(T) + B_{nl,n'l'}^Q(T) \frac{n_{\text{HI}}}{n_p}, \quad (25)$$

¹ Note that the definition here is different from Spitzer (e.g. 1978, § 4.3).

Table 5. Branching ratio, $B_{2,1}^R$, for different transitions for both Case A and Case B.

Line	Case A					Case B				
	$\log T = 3.0$	$\log T = 3.5$	$\log T = 4.0$	$\log T = 4.5$	$\log T = 5.0$	$\log T = 3.0$	$\log T = 3.5$	$\log T = 4.0$	$\log T = 4.5$	$\log T = 5.0$
Balmer α	0.327	0.250	0.178	0.122	0.085	0.995	0.755	0.571	0.441	0.357
Balmer β	0.062	0.057	0.048	0.035	0.025	0.199	0.175	0.148	0.121	0.100
Balmer γ	0.023	0.023	0.020	0.015	0.011	0.076	0.070	0.062	0.052	0.043
Paschen α	0.202	0.135	0.082	0.047	0.028	0.503	0.317	0.192	0.119	0.080
Paschen β	0.048	0.038	0.027	0.017	0.010	0.123	0.092	0.064	0.043	0.031
Brackett α	0.134	0.081	0.044	0.023	0.012	0.324	0.182	0.098	0.054	0.033

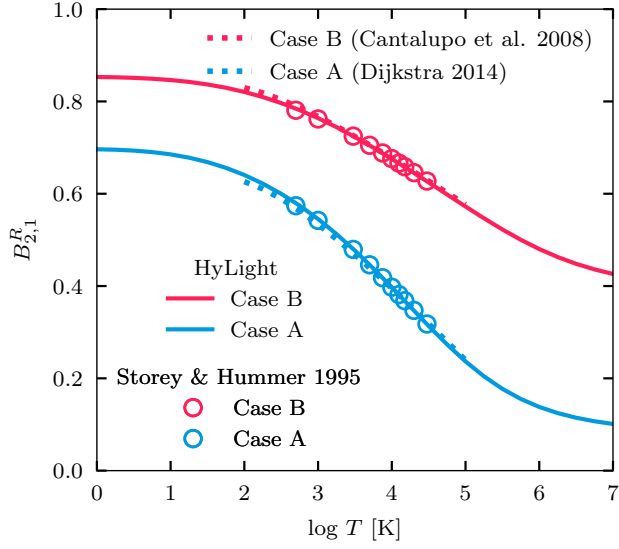


Figure 10. Fraction $B_{2,1}^R$ of the total number of recombinations that result in the emission of a Lyman α photon as a function of temperature, assuming Case A recombinations (blue), or Case B recombinations (red). The HyLight model is shown as drawn lines; the interpolation functions from Cantalupo et al. (2008) and Dijkstra (2014) are shown with dotted lines; discrete Storey & Hummer (1995) values are shown with open circles. All models, including HyLight, ignore collisional excitation, in which case $B_{2,1}^R$ is independent of density. All models agree well with each other.

which shows that the branching ratio is the sum of a term due to recombinations (first term) and a term due to collisions (second term). Summing over l yields the total branching ratio, $B_{n,n'}$, as

$$B_{n,n'}(T) = \sum_{l=0}^{n-1} \sum_{l'=l\pm 1} B_{nl,n'l'}(T) \equiv B_{n,n'}^R(T) + B_{n,n'}^Q(T) \frac{n_{\text{HI}}}{n_p}, \quad (26)$$

with the second line again separating recombinations from collisional excitations.

When collisional excitations are ignored, the emissivity in the transition $n \rightarrow n'$ can be written as

$$\begin{aligned} \epsilon_{n,n'} &= h\nu_{n,n'} B_{n,n'}^R(T) \alpha_{\text{tot}} n_e n_p \\ &\equiv h\nu_{n,n'} \alpha_{n,n'}^{\text{eff}} n_e n_p \\ \alpha_{n,n'}^{\text{eff}} &= B_{n,n'}^R(T) \alpha_{\text{tot}} \end{aligned} \quad (27)$$

The relation between the line emissivity, ϵ , and the effective recombination rate, α^{eff} , was discussed by Osterbrock (1974) (§ 4.3) and

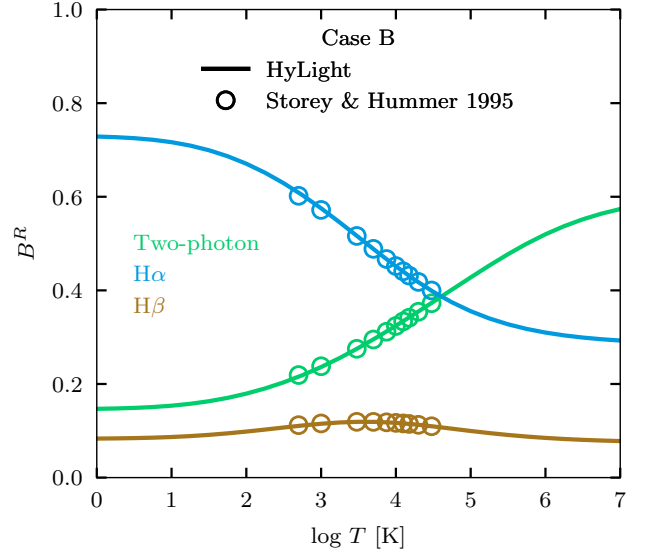


Figure 11. Fraction B^R of the total number of recombinations that result in the emission of selected lines as a function of temperature in Case B. The HyLight model is shown as drawn lines; the results from Storey & Hummer (1995) are shown with open circles. Ignoring collisional excitation from the ground state, both models are in excellent agreement for all three lines, including two-photon emission of the metastable 2s state (green), H α (blue), and H β (brown).

then formally derived by Spitzer (1978) (§ 9.1, table 9.1). Both have used two-photon emission as an example, but the spirit remains the same. With more accurate atomic data available, Cantalupo et al. (2008) derived a fitting formula for Lyman α , i.e. $B_{2,1}^R(T)$, in Case B (accurate in the temperature range 10^2 K $\leq T \leq 10^5$ K based on Pengelly & Seaton 1964a and Martin 1988). The Case A result is also quoted by Dijkstra 2014.

It is straightforward to calculate $B_{n,n'}^R(T)$ and hence the effective recombination coefficient using HyLight. We plot the result in Fig. 10 and Fig. 11 along with the results from Cantalupo et al. 2008, Dijkstra 2014 and Storey & Hummer 1995. The Storey & Hummer 1995 values are evaluated from line emissivities (referred to as R_NU in the original table) based on Equation (27). We also report some numerical values in Table 4 for reference. We find excellent agreement between HyLight and those calculated from Storey & Hummer (1995).

The branching ratio can be used to relate the line luminosity to the total ionization rate for gas in ionization equilibrium. Taking the example of H α , the line luminosity is found by integrating the

emissivity over the volume of the ionised region,

$$\begin{aligned} L_{3,2} &= h\nu_{3,2} \int B_{3,2} n_e n_p \alpha_{\text{tot}} dV \\ &= h\nu_{3,2} B_{3,2}^R \int \alpha_{\text{tot}} n_e n_p dV + h\nu_{3,2} B_{3,2}^Q \int \alpha_{\text{tot}} n_e n_{\text{HI}} dV \\ &\approx h\nu_{3,2} B_{3,2}^R \dot{N}_\gamma. \end{aligned} \quad (28)$$

The last line assumes that the gas is highly ionised, the nebula is radiation bounded, and $B_{3,2}^R n_p \gg B_{3,2}^Q n_{\text{HI}}$ so that the collisional term can be neglected. In addition, it is assumed that $B_{3,2}^R$ is a constant throughout the ionised region, which would be a good approximation if the temperature is approximately uniform. The remaining volume integral is then the total recombination rate in the cloud, which equals the rate at which the source emits ionising photons, \dot{N}_γ , *i.e.* that the gas is in photo-ionisation equilibrium. We can substitute numerical values to find that

$$\dot{N}_\gamma = 2.22 \times 10^{45} \text{ s}^{-1} \frac{L_{3,2}}{L_\odot} = 3.47 \times 10^{44} \text{ s}^{-1} \frac{L_{2,1}}{L_\odot}, \quad (29)$$

thereby relating the ionisation rate to the $\text{H}\alpha$ luminosity ($L_{3,2}$) or Lyman α luminosity ($L_{2,1}$). The numerical values used Case B recombinations and a gas temperature of 10^4 K. Arguably, calculating the Lyman α emissivity in Case B is inconsistent, since Case B assumes that the nebula is optically thick to all Lyman lines. However, the Lyman α emissivity can also be written as

$$L_{2,1} = h\nu_{2,1} \alpha_{\text{B},1s}^{\text{eff}} n_e n_p, \quad (30)$$

where $\alpha_{\text{B},1s}^{\text{eff}}$ is the effective recombination rate for Case B recombinations from Equation (10). The value of $\alpha_{\text{B},1s}^{\text{eff}}$ indeed assumes that the nebula is optically thick to all Lyman lines, but the expression for $L_{2,1}$ assumes that, nevertheless, the $2p$ state decays to $1s$ by emitting a Lyman α photon. Equation (30) is useful for comparing different models with each other, but is not applicable to a physical system (see also §10.3 of the CLOUDY manual).

We can make the model that relates \dot{N}_γ to $L_{3,2}$ more applicable to real HII regions by accounting for dust (see also Hirashita et al. 2003). Consider spherical dust grains with radius r , uniform density by number n , and cross section for absorption of ionising and $\text{H}\alpha$ photons σ_{UV} and σ_{IR} respectively; the source emits ionising photons at a rate \dot{N}_γ with a spectrum with mean energy of an ionising photon $h\nu_{\text{UV}}$. We further assume that gas is fully ionised inside the Strömgren radius R_S , with no ionising photons escaping beyond R_S . The fraction of UV photons absorbed by dust is

$$d_{\text{UV}} = 1 - \exp(-\tau_{\text{UV}}(R_S)), \quad (31)$$

and the fraction of UV-photons that ionise HI , is then $1 - d_{\text{UV}}$. The $\text{H}\alpha$ luminosity is therefore

$$L_{3,2} = (1 - d_{\text{UV}})(1 - d_{\text{IR}}) B_{3,2}^R \dot{N}_\gamma h\nu_{3,2}, \quad (32)$$

where d_{IR} is the fraction of $\text{H}\alpha$ photons absorbed by dust. The dust luminosity is

$$L_{\text{dust}} = d_{\text{UV}} \dot{N}_\gamma h\nu_{\text{UV}}, \quad (33)$$

where we neglect the dust heating by $\text{H}\alpha$ photons compared to that by UV photons. The ratio $L_{3,2}/L_{\text{dust}}$, is

$$\frac{L_{3,2}}{L_{\text{dust}}} = \frac{(1 - d_{\text{UV}})(1 - d_{\text{IR}})}{d_{\text{UV}}} \frac{B_{3,2} \nu_{3,2}}{\nu_{\text{UV}}} \equiv \mathcal{R} \frac{B_{3,2} \nu_{3,2}}{\nu_{\text{UV}}}. \quad (34)$$

The dimensionless variable \mathcal{R} depends on how efficiently the dust absorbs UV-photons compared to $\text{H}\alpha$ photons, but also on the geometry of the nebula. Finally, we can write \dot{N}_γ in terms of the $\text{H}\alpha$ or

dust luminosity, as

$$\begin{aligned} \dot{N}_\gamma &= \frac{L_{3,2}}{\mathcal{R} d_{\text{UV}} B_{3,2} h\nu_{3,2}} \\ &= \frac{L_{\text{dust}}}{d_{\text{UV}} h\nu_{\text{UV}}}. \end{aligned} \quad (35)$$

And hence the total IR luminosity emitted by this dust is

$$L_{\text{dust}} = d_{\text{UV}} \dot{N}_\gamma + (1 - d_{\text{UV}}) d_{\text{IR}} \dot{N}_\gamma h\nu_{3,2}. \quad (36)$$

4.2 Mock integral field data calculated from a simulation

As a second example of HyLIGHT, we post-process the snapshots of a non-equilibrium radiation-hydrodynamical simulation to make mock IFU data cubes in hydrogen emission lines. We choose two set-ups: (1) a spherical, uniform density, HII region with a single central source, with the calculation imposing ionisation equilibrium ('idealised HII region'), and (2) a cubic simulation volume with an initially turbulent density field, irradiated from one side with ionising radiation and accounting for non-equilibrium processes ('turbulent box'). We compare our results for the idealised HII region to CLOUDY, and use the turbulent box simply as an illustration of the power of the atomic model in generating synthetic observations. We begin by briefly reviewing the SPARCS code used to perform the simulations.

4.2.1 SPARCS: a multi-frequency radiation hydrodynamical code

SPARCS is an implementation of a two-moment method for radiative transfer in the SWIFT SPH code (Schaller et al. 2024) as described by Chan et al. (2021) and Chan et al. (2025). This two-moment method, also known as the 'M1' scheme, integrates the first two moments of the radiative transfer equation together with an 'M1' closure relation (Minerbo 1978; Levermore 1984). Radiation is transported between gas particles and each particle stores the local photon flux and density in a set of spectral bins. The bins are typically chosen to include important ionisation thresholds (typically for hydrogen and helium, together with a spectral bin for non-ionising photons).

SPARCS uses the CHIMES² chemistry module (Richings et al. 2014a,b) to update the photon densities, ionisation fractions for all elements and gas temperature. This chemistry module tracks the ionisation states of 157 species, including common molecules. When the ionisation/recombination rates are high, CHIMES sub-cycles this time-step, integrating the equations with the CVODE solver (Cohen et al. 1996)³ for coupled, numerically 'stiff' differential equations. Full details of the coupling between radiation and thermo-chemistry, including tests of the method, are presented by Chan et al. (2025).

4.2.2 Post-processing a simulation with RADMC-3D

Given the ionisation states, density and temperature of each gas particle, as computed using SPARCS, we use HyLIGHT to compute the level population density of the hydrogen atoms for each particle. We can then calculate the number of particles in a specific excited state using Equation (F2). We further feed the information to RADMC-3D⁴ (Dullemond et al. 2012).

RADMC-3D computes the specific intensities emerging from a nebula using Monte Carlo radiative transfer on an adaptively refined

² <https://richings.bitbucket.io/chimes/home.html>

³ <https://computing.llnl.gov/projects/sundials/cvode>

⁴ <https://www.ita.uni-heidelberg.de/~dullemond/software/radmc-3d/>

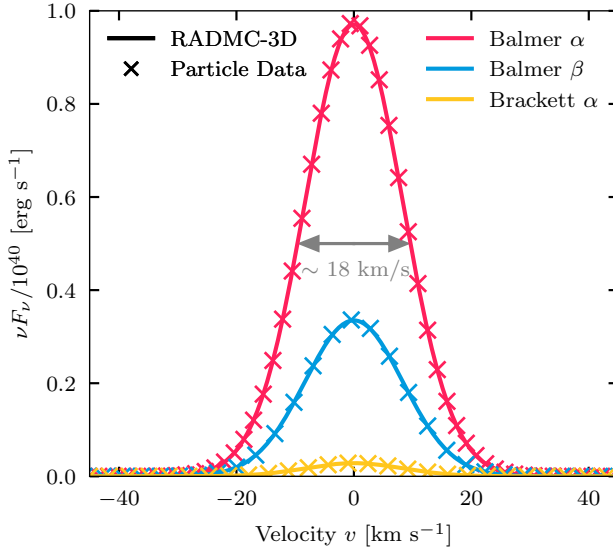


Figure 12. Spectrum of the H α , H β , and Brackett α line (shown in red, blue and yellow) for the idealised H II region described in § 4.2.3. The result from combining the output from the SPARCS simulation with HyLIGHT and RADMC-3D is shown with *solid lines*, the line profile computed directly from the particle data is shown by *crosses*. The total luminosity estimated by RADMC-3D agrees to better than 0.5 per cent with that from the particle data. This demonstrates the consistency of our pipeline for post-processing the simulations with RADMC-3D. A line width ($\sim 18 \text{ km s}^{-1}$) corresponding to gas that emits at a temperature 10^4 K is indicated in the figure to guide the eye.

mesh, accounting for self-absorption and dust attenuation. We interpolate the physical properties of the SPH particles (density, temperature, abundance, level population density) to RADMC-3D’s adaptively refined mesh. Note that we map the number of hydrogen atoms in the excited states onto the AMR grid instead of directly calculating the level population density on the grid (with the interpolated electron density, H II and H I density) to ensure the convergence of total luminosity. The convergence originates from the conservation of particle mass. Refinement of the mesh occurs whenever the minimum smoothing length of the particles within a cell is larger than a fraction of the cell size. This fraction is specified by the user. We verified the convergence of the results in Appendix G. RADMC-3D then performs dust radiative transfer and non-LTE line transfer for specified lines, outputting the result in the form of a mock IFU datacube. The spatial pixel size and wavelength resolution are both specified by the user.

4.2.3 Mocks of an idealised H II region

As a first test case of the combination of SPARCS, HyLIGHT and RADMC-3D, we initialise a cubic computational volume with uniform density and uniform temperature gas (linear extent 22 pc, hydrogen density $n_{\text{H}} = 10 \text{ cm}^{-3}$, gas temperature 10^4 K , initially neutral). The gas is represented with 128^3 SPH particles. A central source emits ionising photons with a blackbody spectrum (ionisation rate $\dot{N}_{\gamma} = 5 \times 10^{47} \text{ s}^{-1}$, blackbody temperature 10^5 K). With these parameters, the H II region is radiation bounded with Strömgren radius $R_S \approx 4.6 \text{ pc}$. This is the same setup as described in § 3.3.2 ‘Multi-frequency H II region with hydrogen, helium, and metals’ of Chan et al. 2025, except for the gas temperature. The simulations track the following elements

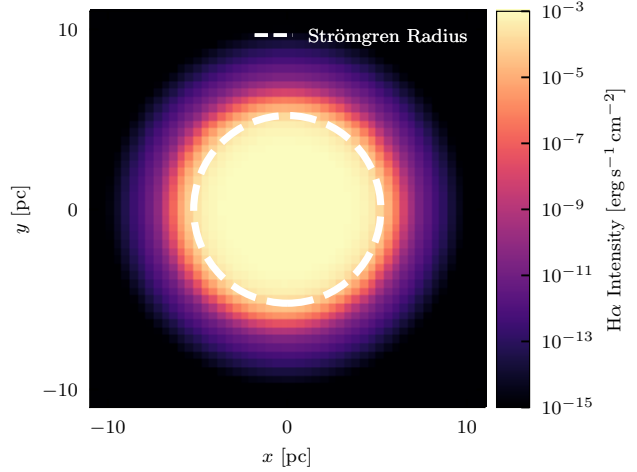


Figure 13. H α intensity of the idealised H II region simulation, computed by integrating the IFU cube obtained from RADMC-3D over wavelength. As expected, H α originates predominantly from the highly ionised gas inside the Strömgren radius ($R_S \approx 4.6 \text{ pc}$), as indicated by the dashed white circle.

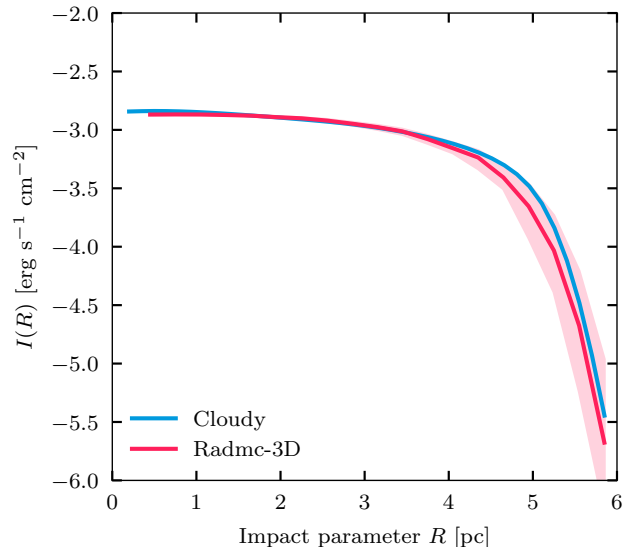


Figure 14. H α surface brightness profile of the idealised H II region simulation. The result from combining SPARCS with HyLIGHT and RADMC-3D are shown in red (where the solid line is the median profile, the shaded region encompasses the 10th ~ 90th percentiles), the CLOUDY result is shown in blue. The two models agree well with each other inside the H II region. There are small differences close to and outside the Strömgren radius, $R_S \approx 4.6 \text{ pc}$, due to non-equilibrium effects in the simulation which are not captured by CLOUDY, which assumes ionisation equilibrium.

and their ions: H, He, C, N, O, Ne, Mg, Si, S, Ca and Fe, with solar abundances as given in table 1 of Wiersma et al. (2009).

Radiative transport is performed using SPARCS with eight frequency bins (with edges [13.60, 18.00, 24.59, 35.50, 54.42, 68.02,

81.62, 95.22, ∞] eV⁵). We turn off gas dynamics, dust, cosmic rays, and molecular physics for simplicity. The simulation is run for 1.2 Myr, by which time the ionization state is nearly in equilibrium and the ionization front is close to the Strömgren radius. During the simulation, we keep the temperature and the density of the gas constant. The test also neglects hydrodynamical effects and examines the cloud in thermal equilibrium, which allows us to compare our results to CLOUDY⁶.

We follow the workflow described in § 4.2.2 to prepare the input files for RADMC-3D. Then we execute line RT in RADMC-3D to obtain a mock spectrum and image of the simulated H II region⁷.

Given our choice of parameters, self-shielding of H α is negligible and since we don't include dust, the luminosity of the cloud is equal to the integral of the emissivity over its volume. We use this to predict the line profile from the particle data by accounting for the temperature of each gas particle, and summing the emission lines of all particles (the line width is approximately 18 km s⁻¹). The gas in the simulation is static, and we do not include an unresolved 'micro-turbulence' component and hence the line width is purely due to thermal broadening. This way, we predict the total luminosity and the line profile directly from the particle data. Comparing this to RADMC-3D provides a test of the interface between SPARCS, HyLIGHT and RADMC-3D.

We compute the luminosity of the H α line for a single particle, i , as

$$L_{3,2,i} = \int \sum_{l=0}^2 \sum_{l'=l\pm 1} n_{3l,i} A_{3l,2l'} h\nu_{3,2} dV \\ \approx \frac{h\nu_{3,2}}{n_{H,i}} \sum_{l=0}^2 \sum_{l'=l\pm 1} n_{3l,i} A_{3l,2l'} \int n_{H,i} dV. \quad (37)$$

Here, $n_{H,i}$ is the hydrogen density of the particle, $n_{3l,i}$ is the population density of the particle in the $n = 3$ excited state (including 3s, 3p, and 3d) - as computed by HyLIGHT - and the integral $\int n_{H,i} dV$ is the total hydrogen mass of the particle. Adding the different allowed transitions yields the total H α luminosity of the particle, and summing that over particles yields the 'particle' estimate of the H α luminosity of the cloud. We assume that the shape of the emission line for each particle is Gaussian with a variance set by the temperature of the particle. Summing over particles yields the spectrum of the cloud. More details on the methodology can be found in Appendix F. We compare the spectrum computed from the particles to that obtained using RADMC-3D in Fig. 12, finding excellent agreement.

We compare the luminosity obtained by (i) total H α luminosity calculated from particles; (ii) relating the ionisation rate to the line luminosity using the branching ratio's described in the previous section; (iii) integrating the luminosity over the line profile computed by RADMC-3D; and (iv) total luminosity predicted by CLOUDY⁸. The total luminosity in the first three cases converges to 6.8×10^{35} erg s⁻¹. The relative difference between (i) and (ii) is smaller than 0.5 per cent; The relative difference between (i) and (iii) is smaller than 1 per cent, whereas the difference between (i) and (iv) is about 5 per cent. The difference comes from the two facts: first, in the setup of CLOUDY used for this comparison, we were not using 100 resolved

⁵ These values correspond or approximately correspond to ionization energies of different ionization stages of H, He, C, N, O.

⁶ The gas temperature is also fixed at 10⁴ K for fair comparison.

⁷ We made use of the spectrum and image commands in RADMC-3D.

⁸ We set up a CLOUDY model with the same ionization source and same element abundance used in SPARCS but with only 30 resolved levels and 10 collapsed due to limitation of computing resources.

levels for hydrogen due to the limitation of the computing resources; second, the simulation is not evolved for long enough for the gas to be in ionisation equilibrium everywhere. This causes small differences in the level prediction between HyLIGHT (which does not impose ionisation equilibrium) and CLOUDY (which does).

Next, we compute the surface brightness of H α by integrating the IFU cube from RADMC-3D over wavelength,

$$I_F(R) = \int F_\lambda(R, \nu) d\lambda, \quad (38)$$

where R is the projected distance to the source, and $F_\lambda d\lambda = F_\nu d\nu$. We plot an image of H α intensity of the nebula in Fig. 13 and the corresponding surface brightness profile in Fig. 14 (red for HyLIGHT, blue for CLOUDY). Although the set-up is spherically symmetric, the SPH realisation of the cloud is not perfectly spherically symmetric due to the underlying particle distribution, which results in a range of I_F values at any given R . The finite pixel size of the image also results in deviations from circular symmetry. The scatter in surface brightness at a given radius is quantified in Fig. 14 by the red hashed region which includes the 10-90th percentile of I_F in bins of R . We compute the corresponding surface brightness from CLOUDY by integrating the H α emissivity along the line of sight,

$$I_C(R) = 2 \int_{r=R}^{r=R_{\max}} \epsilon(r) \frac{r dr}{\sqrt{r^2 - R^2}}, \quad (39)$$

where r is the 3-dimensional distance to the source, and we integrate out to $R_{\max} = 8$ pc. Well inside R_S , the HyLIGHT surface brightness, I_F , agrees well with the CLOUDY value, I_C . Close to and outside R_S , the curves differ, which is partially because the simulated nebula is not yet fully in ionization equilibrium.

In summary: we have computed the emissivity of a simple H II region with SPARCS, post-processing the simulation with HyLIGHT and RADMC-3D. We find excellent agreement with CLOUDY in terms of the line luminosities of hydrogen recombination lines, and of the corresponding surface brightness profile.

4.2.4 Mocks of an illuminated turbulent density field

We illustrate the flexibility of our modelling by the following more realistic version of a small patch of a dynamical H II region with an initially inhomogeneous density structure, and gravity. The setup is described in more detail in section 4 of Chan et al. 2025. Briefly, we set up a cubic simulation volume with a linear extent of 1 pc with 128³ gas particles, initially at uniform density and uniform temperature, (hydrogen number density $\langle n_H \rangle = 50$ cm⁻³, $T = 15$ K) and the same solar abundance pattern as in the previous section. The gas is initially neutral.

Inhomogeneities are introduced by driving isothermal solenoidal turbulence with a Mach number of five, using the PHANTOM SPH code described by Price et al. (2018). The turbulence is driven over five crossing times, and we use the particle distribution at the end of the PHANTOM run as the initial condition for SPARCS; the initial gas velocity is set to zero everywhere.

We inject ionizing radiation with a blackbody spectrum (temperature 3×10^4 K) in the form of plane-parallel radiation that is propagating perpendicular to the $x = 0$ plane of the computational volume. The flux of ionising photons at the edge is taken to be 2×10^{10} cm⁻² s⁻¹. We also include low-energy cosmic ray heating and ionisation, both of which are also implemented in CHIMES.

Our results are illustrated by Fig. 15, where the grey buffer region at $x > 0.8$ pc is where we remove photons to avoid the periodic boundary conditions artificially enhancing the radiation inside the

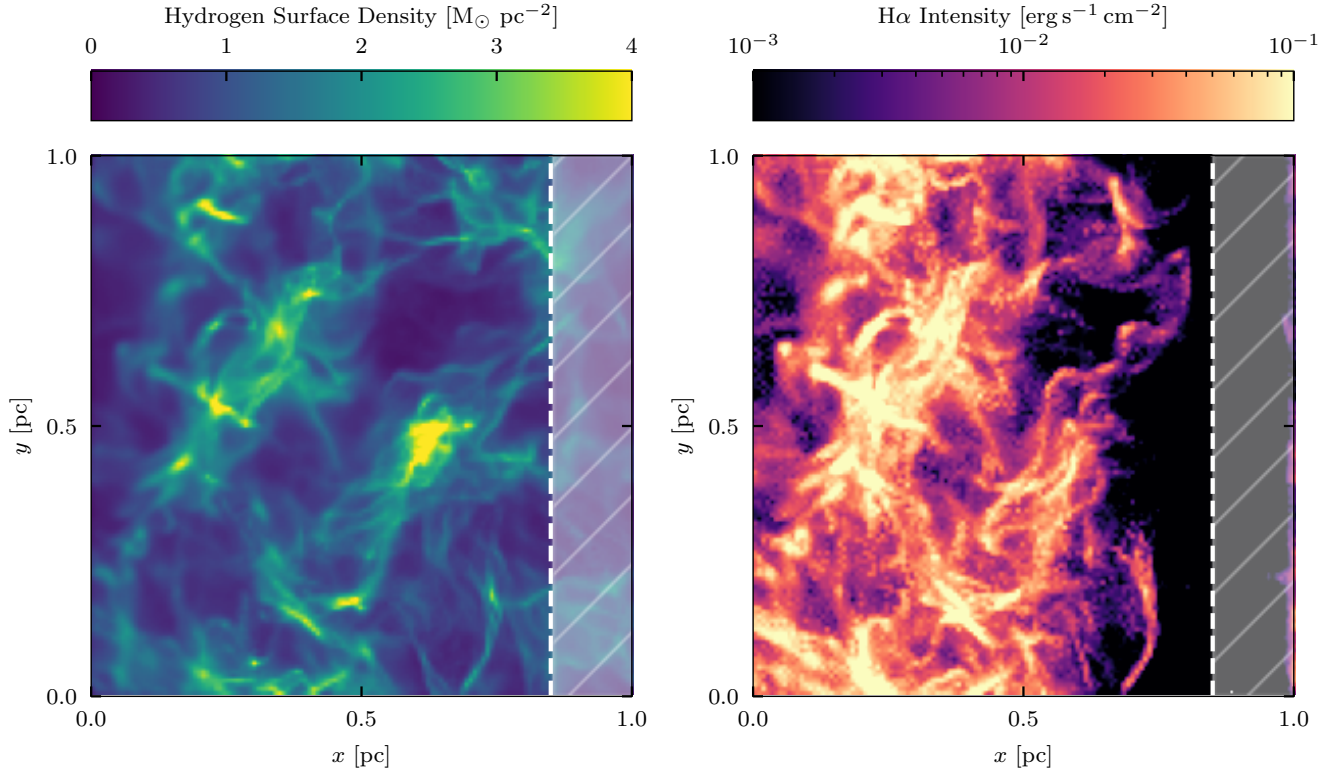


Figure 15. Surface density of hydrogen gas (left panel) and H α intensity (right panel) for the case of an initially turbulent density field. Ionising radiation is injected perpendicular to the $x = 0$ plane, with SPARCS propagating the radiation to the right. Photons are removed from the radiation field for $x > 0.8$ pc (grey dashed regions in both panels) to avoid effects of periodic boundary conditions. The hydrogen surface density is obtained by integrating the total hydrogen density (the sum of H I and H II) along the z -axis. The H α surface brightness is calculated by combining HyLIGHT with RADMC-3d. The filamentary pattern resulting from the turbulent driving seen in the density field (left panel) is reflected in the H α intensity map (right panel).

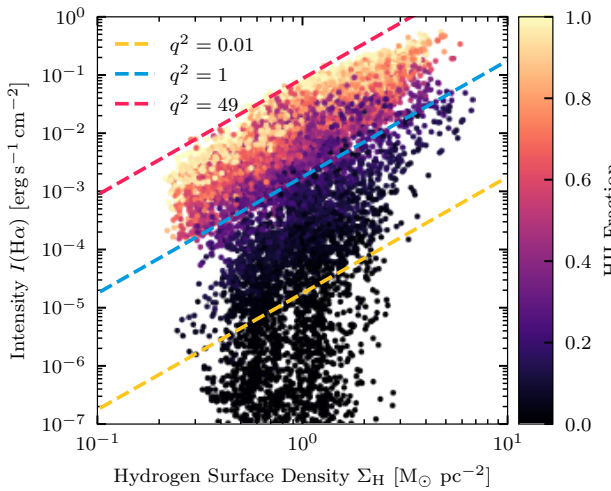


Figure 16. Relation between hydrogen surface density, Σ_{H} , and H α surface brightness, $I(\text{H}\alpha)$, for the simulation of Fig. 15. Each point corresponds to a pixel, with points coloured by the mean ionised fraction along the sight line. The dashed lines indicate the relation of Equation (40), with q being a dimensionless parameter measuring the mean ionised fraction. These trend lines capture the colour shading of the pixels.

volume. The left panel illustrates the total hydrogen column density at the start of the simulation; the filamentary regions with high column density are due to the turbulent driving. Given the ionisation states from SPARCS, we use HyLIGHT to compute the level population of H I , and finally RADMC-3d to compute the H α surface brightness (right panel). Regions with high H I density are also high in H α surface brightness, and the filamentary high-density regions in the gas create filaments of high H α emissivity.

We further investigate the correlation between H α surface brightness and hydrogen surface density in Fig. 16: for each pixel (given values of x and y) in Fig. 15, we plot the hydrogen column density from the left panel, Σ_{H} , against the H α surface brightness from the right panel, $I(\text{H}\alpha)$, with points coloured according to the mean ionised fraction. Drawn lines show the power law,

$$I(\text{H}\alpha) = \frac{q^2 h \nu_{3,2} \langle \alpha_{3,2}^{\text{eff}} \rangle}{m_{\text{H}}^2 L} \Sigma_{\text{H}}^2, \quad (40)$$

where $h \nu_{3,2}$ is the energy of an H α photon, m_{H} is the mass of a hydrogen atom, $\langle \alpha_{3,2}^{\text{eff}} \rangle$ is the average effective rate of emission of H α photons defined by Equation (27), and $L = 1$ pc is the length of the simulation volume; different lines correspond to different values of the dimensionless parameter q . These lines capture the trend seen in the coloured points of increasing $I(\text{H}\alpha)$ with increasing Σ_{H} at constant H II fraction.

The origin of the correlation expressed by Equation (40) can be understood as follows: firstly, the H α surface brightness is an integral

of the $\text{H}\alpha$ emissivity, $\epsilon_{3,2}$, along the z -axis,

$$\begin{aligned} I(\text{H}\alpha) &= \int \epsilon_{3,2} dz \\ &= h\nu_{3,2} \int n_p n_e \alpha_{3,2}^{\text{eff}} dz \\ &\approx h\nu_{3,2} \langle x_{\text{HII}} \rangle^2 \langle \alpha_{3,2}^{\text{eff}} \rangle \int n_{\text{H}}^2 dz \\ &\equiv h\nu_{3,2} \langle x_{\text{HII}} \rangle^2 \langle \alpha_{3,2}^{\text{eff}} \rangle L \langle n_{\text{H}}^2 \rangle. \end{aligned} \quad (41)$$

The first step used Equation (27), the second step defined $\langle x_{\text{HII}} \rangle$ to be the mean ionized fraction and $\langle \alpha_{3,2}^{\text{eff}} \rangle$ the mean effective rate of emission of $\text{H}\alpha$ photons, and the final step defined

$$\langle n_{\text{H}}^2 \rangle = \frac{1}{L} \int n_{\text{H}}^2 dz. \quad (42)$$

Defining

$$\langle n_{\text{H}} \rangle = \frac{1}{L} \int n_{\text{H}} dz = \frac{\Sigma_{\text{H}}}{L}, \quad (43)$$

and setting $q^2 = \langle x_{\text{HII}} \rangle^2 \langle n_{\text{H}}^2 \rangle / \langle n_{\text{H}} \rangle^2$ yields Equation (40).

Equation (40) shows that, at a constant q (given level of ionization, given level of density inhomogeneity, $\langle n_{\text{H}}^2 \rangle / \langle n_{\text{H}} \rangle^2$), $I(\text{H}\alpha) \propto \Sigma_{\text{H}}^2$. Decreasing the level of inhomogeneity, or the level of ionization, decreases $I(\text{H}\alpha)$ for a given value of Σ_{H}^2 - this is what we see in Fig. 16.

5 CONCLUSIONS

Hydrogen recombination lines play a crucial role in the emission line diagnostics used to infer physical conditions of nebular regions and the interstellar medium (ISM) of galaxies. Forward models of the ISM, based on hydrodynamical simulations that include radiative transfer, need to be post-processed to compute the strength of the hydrogen emission lines to enable a direct comparison to observations. This post-processing step requires a model that predicts the level population in HI , since hydrogen emission lines arise from transitions from excited states to more bound states.

We have compared predictions for the level population as a function of density and temperature between several models (such as that of [Raga et al. 2015](#) and [CLOUDY Ferland et al. 2017; Gunasekera et al. 2023](#)), as well as values from published tables ([Storey & Hummer 1995](#)), and find values that differ by factors of several, even for common lines such as $\text{H}\alpha$ and $\text{H}\beta$ (see § 2). We also find that the [CLOUDY](#) prediction using the default choice of parameters for the number of energy levels included in the calculation, can be off from the numerically converged answer by 10s of per cent. Tabulated values cannot be used to investigate the level population in case the gas is not in ionisation equilibrium, and the same holds for the [CLOUDY](#) predictions, which assume ionisation balance. However, numerical simulations are able to integrate the rate equations and can hence account for non-equilibrium effects. The disagreement of energy levels between different models, and the fact that most of these models cannot account for non-equilibrium effects, motivated us to develop [HyLIGHT](#). This [PYTHON](#) code determines the level population of HI , given the temperature, density, and ionisation state of the gas. The latter can be computed by radiation-hydrodynamic simulation that includes non-equilibrium effects, for example, using the [SPARCS](#) code described by [Chan et al. \(2025\)](#).

The [HyLIGHT](#) model accounts for the dominant mechanisms that determine the level population under nebular conditions, namely recombinations and collisional excitation from the ground state: the

model is described in § 3. [HyLIGHT](#) is implemented in [PYTHON](#) and is publicly available. The level population levels and emissivity predicted by [HyLIGHT](#) agree with those from [CLOUDY](#) (version C23.02) at the per cent level or better, when the gas is assumed to be in ionisation equilibrium. § 3 also investigates the minimum number of levels the model should include in order to converge. [HyLIGHT](#) serves as a stand-alone package for the accurate calculation of hydrogen line emission, and is easy to integrate into other codes or post-processing pipelines for analysing simulation snapshots.

We present two applications of [HyLIGHT](#) in § 4. We first use the model to compute branching ratios - the ratio of the rates at which HI ions transition between two levels $n \rightarrow n'$ (where n is the principal quantum number) over the total recombination rate. Such a branching ratio can be used to relate the photo-ionisation rate in a radiation-bound HII region to line luminosity such as that of the $\text{H}\alpha$ line (see Equation (29)).

In the second application, we post-process simulations performed with the [SPARCS](#) code ([Chan et al. 2025](#)). One simulation is that of a spherically symmetric, uniform, radiation-bound HII region, which is ionised by a time-independent central source. We feed the simulation output to [HyLIGHT](#) to determine the level population, and feed the output of that calculation into [RADMC-3D](#) [Dullemond et al. \(2012\)](#) to compute an $\text{H}\alpha$ surface intensity map. Because the set-up is simple, we can compute the $\text{H}\alpha$ surface brightness profile with [CLOUDY](#) as well, and we find excellent agreement between the two methods.

In a second simulation, we use [SPARCS](#) to compute the evolution of a patch of ISM, with initial density perturbations generated by turbulent driving, which is overrun by an initially plane-parallel ionisation front. The calculation is performed in full non-equilibrium, by taking advantage of the [CHIMES](#) ([Richings et al. 2014a,b](#)) photo-chemistry solver coupled to radiative transfer in [SPARCS](#). We show how regions of high $\text{H}\alpha$ surface brightness correspond to regions with high hydrogen surface density, as might have been expected. Such calculations can be used to investigate the extent to which density structure in a cloud affects the interpretation of line ratio diagrams, where different lines may originate from spatially distinct parts of the cloud.

[HyLIGHT](#) paves the way for examining emission line diagnostics using simulations. It enables examining the impact of feedback and the presence of metals on the emission line diagnostics in the ISM. The method also enables us to compare future simulations of HII regions against spatially resolved observations, e.g., nearby star-forming regions observed by [MUSE](#) ([McLeod et al. 2019](#)). The mock IFU data cubes from our novel simulations contain rich information about the gas properties and will be compared to observations, allowing us to investigate the spatially resolved observations from a new perspective. In addition, our calculation is not restricted to equilibrium solutions of the system. The method applies to studies of the non-equilibrium evolution of the ISM and even on-the-fly radiative cooling in the future.

ACKNOWLEDGEMENTS

We thank Peter van Hoof and the [CLOUDY](#) discussion forum for helpful discussions.

This work is co-funded by the European Union (Widening Participation, ExGal-Twin, GA 101158446). Views and opinions expressed are however those of the author(s) only and do not necessarily reflect those of the European Union. Neither the European Union nor the granting authority can be held responsible for them. This work

received funding from the Horizon Europe guarantee scheme of UK Research and Innovation (UKRI).

We acknowledge the support of the DiRAC@Durham facility managed by the Institute for Computational Cosmology on behalf of the STFC DiRAC HPC Facility (www.dirac.ac.uk). The equipment was funded by BEIS capital funding via STFC capital grants ST/K00042X/1, ST/P002293/1, ST/R002371/1 and ST/S002502/1, Durham University and STFC operations grant ST/R000832/1. DiRAC is part of the National e-Infrastructure.

YKL acknowledges the support from the Durham Doctoral Studentship (DDS).

TKC is supported by the ‘Improvement on Competitiveness in Hiring New Faculties’ Funding Scheme (4937210-4937211-4937212), the Direct Grant project (4053662,4443786,4053719) from the Chinese University of Hong Kong, and the RGC Early Career Scheme (24301524). TKC was supported by the E. Margaret Burbidge Prize Postdoctoral Fellowship from the Brinson Foundation at the Departments of Astronomy and Astrophysics at the University of Chicago.

The research in this paper made use of the SWIFT open-source simulation code (<http://www.swiftsim.com>, Schaller et al. 2024). The analysis made use of MATPLOTLIB (Hunter 2007), NUMPY (Harris et al. 2020), SCIPY (Jones et al. 01 ; Virtanen et al. 2020), SWIFT-SIMIO (Borrow & Borrisov 2020), UNYT (Goldbaum et al. 2018), h5PY (Collette et al. 2022) and PANDAS (McKinney 2010; The pandas development team 2020). We also made use of the arXiv preprint service and NASA’s Astrophysics Data System.

DATA AVAILABILITY

The HyLight package is publicly available at <https://github.com/YuankangLiu/HyLight>. The CLOUDY code is available at <https://gitlab.nublado.org/cloudy/cloudy/-/wikis/home>. The FORTRAN 77 code to calculate Einstein A values can be found at <https://data.mendeley.com/datasets/3drgznwty8/1>. The public version of the SWIFT code is available at <http://www.swiftsim.com>, which includes the SPH-M1RT radiative transfer module coupled with a simple hydrogen and helium thermo-chemistry network. The CHIMES code and the associated package are publicly available at <https://richings.bitbucket.io/chimes/home.html>. Currently, SPARCS is a SWIFT module located in a private SWIFT branch. SPARCS will be released to the public in the future. RADMC-3D is publicly available at <https://www.ita.uni-heidelberg.de/~dullemond/software/radmc-3d/>. The input scripts for the CLOUDY models and the analysis code used in this paper can be accessed at <https://doi.org/10.5281/zenodo.16911175>.

REFERENCES

Anderson H., Ballance C. P., Badnell N. R., Summers H. P., 2000, *Journal of Physics B: Atomic, Molecular and Optical Physics*, 33, 1255

Anderson H., Ballance C. P., Badnell N. R., Summers H. P., 2002, *Journal of Physics B: Atomic, Molecular and Optical Physics*, 35, 1613

Arfken G., Weber H.-J., Harris F. E., 2013, *Mathematical Methods for Physicists: A Comprehensive Guide*, 7th ed edn. Elsevier, Amsterdam Boston

Baker J. G., Menzel D. H., 1938, *The Astrophysical Journal*, 88, 52

Baldwin J. A., Phillips M. M., Terlevich R., 1981, *Publications of the Astronomical Society of the Pacific*, 93, 5

Bethe H., Hund F., Mott N. F., Pauli W., Rubinowicz A., Wentzel G., Smekal A., eds, 1933, *Quantentheorie*. Springer Berlin Heidelberg, Berlin, Heidelberg, doi:10.1007/978-3-642-52619-0

Borrow J., Borrisov A., 2020, *Journal of Open Source Software*, 5, 2430

Bottorff M. C., Ferland G. J., Straley J. P., 2006, *Publications of the Astronomical Society of the Pacific*, 118, 1176

Brocklehurst M., 1971, *Monthly Notices of the Royal Astronomical Society*, 153, 471

Cantalupo S., Porciani C., Lilly S. J., 2008, *The Astrophysical Journal*, 672, 48

Chan T. K., Theuns T., Bower R., Frenk C., 2021, *Monthly Notices of the Royal Astronomical Society*, 505, 5784

Chan T. K., Richings A. J., Theuns T., Liu Y., Schaller M., Ivkovic M., 2025, arXiv e-prints, p. arXiv:2508.13277

Chluba J., Sunyaev R. A., 2006, *Astronomy & Astrophysics*, 446, 39

Cohen S. D., Hindmarsh A. C., Dubois P. F., 1996, *Computers in Physics*, 10, 138

Collette A., et al., 2022, h5py/h5py: 3.7.0, doi:10.5281/zenodo.6575970, <https://doi.org/10.5281/zenodo.6575970>

D’Agostino J. J., Kewley L. J., Groves B., Byler N., Sutherland R. S., Nicholls D., Leitherer C., Stanway E. R., 2019, *The Astrophysical Journal*, 878, 2

Dijkstra M., 2014, *Publications of the Astronomical Society of Australia*, 31, e040

Dopita M. A., Sutherland R. S., 1996, *The Astrophysical Journal Supplement Series*, 102, 161

Drory N., et al., 2024, *The Astronomical Journal*, 168, 198

Dullemond C. P., Juhasz A., Pohl A., Sereshti F., Shetty R., Peters T., Commercon B., Flock M., 2012, RADMC-3D: A multi-purpose radiative transfer tool, *Astrophysics Source Code Library*, record ascl:1202.015

Ferland G. J., Peterson B. M., Horne K., Welsh W. F., Nahar S. N., 1992, *The Astrophysical Journal*, 387, 95

Ferland G. J., van Hoof P. A. M., Chatzikos M., Gunasekera C. M., Chakraborty P., Shaw G., Dehghanian M., 1999, *Astrophysics Source Code Library*, p. ascl:9910.001

Ferland G. J., et al., 2017, The 2017 Release Cloudy, doi:10.48550/arXiv.1705.10877

Goldbaum N. J., ZuHone J. A., Turk M. J., Kowalik K., Rosen A. L., 2018, *Journal of Open Source Software*, 3, 809

Gordon W., 1929, *Annalen der Physik*, 394, 1031

Grinin A., Matveev A., Yost D. C., Maisenbacher L., Wirthl V., Pohl R., Hänsch T. W., Udem T., 2020, *Science*, 370, 1061

Groves B., et al., 2023, *Monthly Notices of the Royal Astronomical Society*, 520, 4902

Grudić M. Y., Guszejnov D., Hopkins P. F., Offner S. S. R., Faucher-Giguère C.-A., 2021, *Monthly Notices of the Royal Astronomical Society*, 506, 2199

Gunasekera C. M., Van Hoof P. A. M., Chatzikos M., Ferland G. J., 2023, *Research Notes of the AAS*, 7, 246

Guzmán F., Chatzikos M., van Hoof P. A. M., Balser D. S., Dehghanian M., Badnell N. R., Ferland G. J., 2019, *Monthly Notices of the Royal Astronomical Society*, 486, 1003

Guzmán F., Chatzikos M., Ferland G. J., 2025, *Monthly Notices of the Royal Astronomical Society*, 539, 2939

Harris C. R., et al., 2020, *Nature*, 585, 357

Hirashita H., Buat V., Inoue A. K., 2003, *Astronomy & Astrophysics*, 410, 83

Hirschmann M., Charlot S., Feltre A., Naab T., Choi E., Ostriker J. P., Somerville R. S., 2017, *Monthly Notices of the Royal Astronomical Society*, 472, 2468

Hirschmann M., Charlot S., Feltre A., Naab T., Somerville R. S., Choi E., 2019, *Monthly Notices of the Royal Astronomical Society*, 487, 333

Hirschmann M., Charlot S., Somerville R. S., 2023a, *Monthly Notices of the Royal Astronomical Society*, 526, 3504

Hirschmann M., et al., 2023b, *Monthly Notices of the Royal Astronomical Society*, 526, 3610

Hoang-Binh D., 1990, *Astronomy and Astrophysics*, 238, 449

Hoang-Binh D., 2005, *Computer Physics Communications*, 166, 191

Hummer D. G., Storey P. J., 1987, *Monthly Notices of the Royal Astronomical Society*, 224, 801

Hummer D. G., Storey P. J., 1992, *Monthly Notices of the Royal Astronomical Society*, 254, 277

Hunter J. D., 2007, *Computing in Science & Engineering*, 9, 90

Isobe Y., et al., 2025, *Monthly Notices of the Royal Astronomical Society*:

Letters, 541, L71

Jin Y., Kewley L. J., Sutherland R., 2022, *The Astrophysical Journal*, 927, 37

Jones E., Oliphant T., Peterson P., et al., 2001–, SciPy: Open source scientific tools for Python, <http://www.scipy.org/>

Katz H., 2022, *Monthly Notices of the Royal Astronomical Society*, 512, 348

Kauffmann G., et al., 2003, *Monthly Notices of the Royal Astronomical Society*, 346, 1055

Kennicutt R. C., 1998, *Annual Review of Astronomy and Astrophysics*, 36, 189

Kewley L. J., Dopita M. A., 2002, *The Astrophysical Journal Supplement Series*, 142, 35

Kewley L. J., Dopita M. A., Sutherland R. S., Heisler C. A., Trevena J., 2001, *The Astrophysical Journal*, 556, 121

Kewley L. J., Nicholls D. C., Sutherland R. S., 2019, *Annual Review of Astronomy and Astrophysics*, 57, 511

Labzowsky L., Solovyev D., Plunien G., Soff G., 2006, *The European Physical Journal D*, 37, 335

Lebedev V. S., Beigman I. L., 1998, Physics of Highly Excited Atoms and Ions. Springer Berlin Heidelberg, Berlin, Heidelberg, doi:10.1007/978-3-642-72175-5

Levermore C., 1984, *Journal of Quantitative Spectroscopy and Radiative Transfer*, 31, 149

Luridiana V., Simón-Díaz S., Cerviño M., Delgado R. M. G., Porter R. L., Ferland G. J., 2009, *The Astrophysical Journal*, 691, 1712

Lykins M. L., et al., 2015, *The Astrophysical Journal*, 807, 118

Marino R. A., et al., 2013, *Astronomy & Astrophysics*, 559, A114

Martin P. G., 1988, *The Astrophysical Journal Supplement Series*, 66, 125

McClymont W., et al., 2025, arXiv e-prints, p. arXiv:2503.04894

McKinney W., 2010, in Python in Science Conference. Austin, Texas, pp 56–61, doi:10.25080/Majora-92bf1922-00a

McLeod A. F., Dale J. E., Ginsburg A., Ercolano B., Gritschneider M., Ramsay S., Testi L., 2015, *Monthly Notices of the Royal Astronomical Society*, 450, 1057

McLeod A. F., et al., 2016, *Monthly Notices of the Royal Astronomical Society*, 462, 3537

McLeod A. F., Dale J. E., Evans C. J., Ginsburg A., Kruijssen J. M. D., Pellegrini E. W., Ramsay S. K., Testi L., 2019, *Monthly Notices of the Royal Astronomical Society*, 486, 5263

McLeod A. F., et al., 2021, *Monthly Notices of the Royal Astronomical Society*, 508, 5425

Menzel D. H., 1937, *The Astrophysical Journal*, 85, 330

Menzel D. H., Baker J. G., 1937, *The Astrophysical Journal*, 86, 70

Minerbo G. N., 1978, *Journal of Quantitative Spectroscopy and Radiative Transfer*, 20, 541

Morisset C., 2013, Astrophysics Source Code Library, p. ascl:1304.020

Nussbaumer H., Schmutz W., 1984, *Astronomy and Astrophysics*, 138, 495

Osterbrock D. E., 1974, *Astrophysics of Gaseous Nebulae*

Osterbrock D. E., Ferland G. J., 2006, *Astrophysics of gaseous nebulae and active galactic nuclei*

Peimbert M., 1967, *The Astrophysical Journal*, 150, 825

Pellegrini E. W., Oey M. S., Winkler P. F., Points S. D., Smith R. C., Jaskot A. E., Zastrow J., 2012, *The Astrophysical Journal*, 755, 40

Pengelly R. M., Seaton M. J., 1964a, *Monthly Notices of the Royal Astronomical Society*, 127, 145

Pengelly R. M., Seaton M. J., 1964b, *Monthly Notices of the Royal Astronomical Society*, 127, 165

Perez-Montero E., 2014, *Monthly Notices of the Royal Astronomical Society*, 441, 2663

Pérez-Montero E., 2017, *Publications of the Astronomical Society of the Pacific*, 129, 043001

Pérez E., González Delgado R., Vilchez J. M., 2001, *Astrophysics and Space Science*, 277, 83

Price D. J., et al., 2018, *Publications of the Astronomical Society of Australia*, 35, e031

Raga A. C., Castellanos-Ramírez A., Esquivel A., Rodríguez-González A., Velázquez P. F., 2015, *Revista Mexicana de Astronomía y Astrofísica*, 51, 231

Richings A. J., Schaye J., Oppenheimer B. D., 2014a, *Monthly Notices of the Royal Astronomical Society*, 440, 3349

Richings A. J., Schaye J., Oppenheimer B. D., 2014b, *Monthly Notices of the Royal Astronomical Society*, 442, 2780

Richings A. J., Faucher-Giguère C.-A., Stern J., 2021, *Monthly Notices of the Royal Astronomical Society*, 503, 1568

Richings A. J., Faucher-Giguère C.-A., Gurvich A. B., Schaye J., Hayward C. C., 2022, *Monthly Notices of the Royal Astronomical Society*, 517, 1557

Rodríguez-González A., Peña M., Hernández-Martínez L., Ruiz-Escobedo F., Raga A., Stasińska G., Castorena J. I., 2023, *The Astrophysical Journal*, 955, 151

Rousseau-Nepton L., et al., 2019, *Monthly Notices of the Royal Astronomical Society*, 489, 5530

Rubin R. H., 1989, *The Astrophysical Journal Supplement Series*, 69, 897

Rybicki G. B., Lightman A. P., 1979, Radiative processes in astrophysics

Sankrit R., Hester J. J., 2000, *The Astrophysical Journal*, 535, 847

Schaller M., et al., 2024, *Monthly Notices of the Royal Astronomical Society*, 530, 2378

Seaton M. J., 1959, *Monthly Notices of the Royal Astronomical Society*, 119, 90

Seaton M. J., Osterbrock D. E., 1957, *The Astrophysical Journal*, 125, 66

Shapley A. E., et al., 2025, *The Astrophysical Journal*, 980, 242

Silva B. M., Zaroubi S., Kooistra R., Cooray A., 2018, *Monthly Notices of the Royal Astronomical Society*, 475, 1587

Simpson J. P., Rubin R. H., Colgan S. W. J., Erickson E. F., Haas M. R., 2004, *The Astrophysical Journal*, 611, 338

Spitzer L., 1978, Physical processes in the interstellar medium, doi:10.1002/9783527617722.

Storey P. J., Hummer D. G., 1988, *Monthly Notices of the Royal Astronomical Society*, 231, 1139

Storey P. J., Hummer D. G., 1995, *Monthly Notices of the Royal Astronomical Society*, 272, 41

Sutherland R., Dopita M., Binette L., Groves B., 2018, *Astrophysics Source Code Library*, p. ascl:1807.005

The pandas development team 2020, pandas-dev/pandas: Pandas, doi:10.5281/zenodo.3509134, <https://doi.org/10.5281/zenodo.3509134>

Van Regemorter H., 1962, *The Astrophysical Journal*, 136, 906

Veilleux S., Osterbrock D. E., 1987, *The Astrophysical Journal Supplement Series*, 63, 295

Virtanen P., et al., 2020, *Nature Methods*, 17, 261

Vriens L., Smeets A. H. M., 1980, *Physical Review A*, 22, 940

Vrinceanu D., Flannery M. R., 2001, *Physical Review A*, 63, 032701

Vrinceanu D., Onofrio R., Oonk J. B. R., Salas P., Sadeghpour H. R., 2019, *The Astrophysical Journal*, 879, 115

Walch S., et al., 2015, *Monthly Notices of the Royal Astronomical Society*, 454, 246

Wiersma R. P. C., Schaye J., Theuns T., Dalla Vecchia C., Tornatore L., 2009, *Monthly Notices of the Royal Astronomical Society*, 399, 574

APPENDIX A: CONVERGENCE IN CLOUDY MODELS

We have used CLOUDY models to investigate the hydrogen level population and recombination line emissivity in photoionized regions. Yet it is not obvious that the CLOUDY models converge as the number of resolved levels in the built-in atomic model increases. In Fig. A1, we show the convergence for selected transitions with an increasing number of resolved levels in CLOUDY. We choose the reference ‘Ref - ALSh’ setup in Table 1 but varying the number of resolved levels, n_{res} . Note that we have used the same reference model as in Fig. 3. As the number of resolved levels increases, the emissivities (for all three lines) converge to the reference model. We also indicate the emissivity predictions from the default atomic model (‘Def - ALSh’) which includes 10 resolved levels and 15 collapsed levels. A significant difference between the default model and the reference model

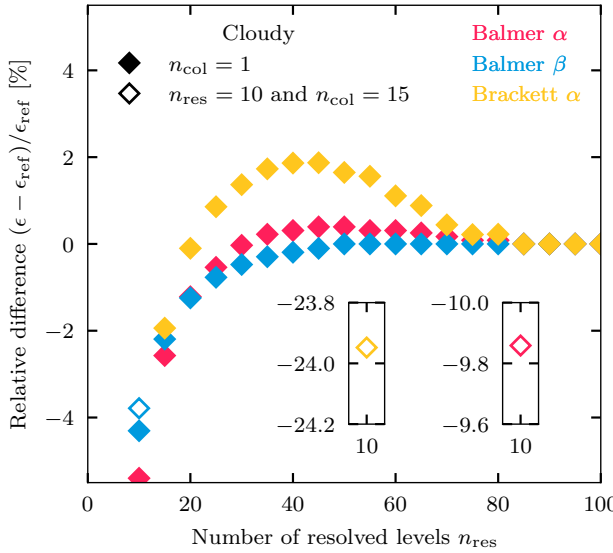


Figure A1. Convergence of emissivity for selected transitions for different CLOUDY models in Case A. The reference setup is ‘Ref - ALSH’ with 100 resolved levels. The solid symbols indicate models with different numbers of resolved levels while keeping only one collapsed level. The open symbols indicate the default setup, i.e. 15 resolved levels and 10 collapsed ones. The emissivities of the selected lines gradually converge to the reference model. We conclude that 100 resolved levels in CLOUDY are sufficient for a convergence. Note that the default model can differ significantly: for $H\alpha$, the difference is about 10%; for $H\beta$, the difference is around 4%; for Brackett α , the difference can be as high as 24%.

can be seen: for Brackett α , the difference is approximately 24%. This finding is similar to that in Guzmán et al. 2025.

The convergence of ‘Ref - ALSH’ model is different from that of ‘Ref - ALSH - RR’ (see Fig. 3). The differences stem from the different processes included in the model. In CLOUDY, users have the freedom to turn on or off different physical processes depending on the aim of the research. Yet these processes have an impact on the level populations of atomic states, leading to different emissivity predictions. Here, we show such impact by studying two major processes - collisional processes (collisional excitation, collisional deexcitation and l -changing collision) and the ‘topoff’ process. In the case of running CLOUDY models with a limited number of resolved levels, the residual recombination coefficients of the higher levels (i.e. collapsed levels) sometimes may not be negligible. The ‘topoff’ command in CLOUDY allows the user to conserve the total radiative recombination coefficient by distributing the residual recombination coefficients into collapsed levels. We show the convergence of level population predictions as a function of the number of resolved levels for various setups in Fig. A2. Four different setups are shown: the radiative-only calculations include only radiative processes; the ‘radiative & topoff’ setup conserves the total recombination coefficient on top of radiative-only calculations; the ‘radiative & collisional’ setup adds collisional processes on top of radiative processes; finally, ‘radiative & topoff & collisional’ contains all four processes. In Fig. A2, the $6s$ level population converges for all four setups while the $6h$ level population does not, despite there being 100 resolved levels already. We conclude that various physical processes have an impact on the convergence of the level population, and different l -states require different numbers of resolved levels to achieve convergence.

Furthermore, we study the impact of the number of collapsed levels on the line emissivity and level population. In Fig. A3 and Fig. A4, we show the convergence of the level population of all the l -states in $n = 6$ and the emissivity of several transitions as a function of the number of collapsed levels. In both figures, we use ‘Ref - ALSH’ (see Table 1) with 100 resolved levels and 1 collapsed level as the reference model. In Fig. A3, we fix the number of resolved levels to 40, while in Fig. A4 we use 100 resolved levels. Not all the level populations have reached convergence with more collapsed levels. Since the emissivity is dependent on various l -states, none of the line emissivities has reached convergence. Increasing the number of resolved levels does not help ease the issue, as is shown in Fig. A4, where we have 100 resolved levels.

APPENDIX B: EINSTEIN A VALUES

Large amounts of Einstein A values are needed for our atomic model. In this work, we utilise a method of calculation of Einstein coefficients up to principle quantum number $n \approx 1000$, which is described in Hoang-Binh (1990) and Hoang-Binh (2005). We summarise the method below.

For a hydrogen atom, the dipole moment corresponding to the transition from the state (n, l) to the state (n', l') is

$$R(n, l; n', l') = \int_0^\infty P_{n,l}(r) r^3 P_{n',l'}(r) dr, \quad (B1)$$

where $P_{n,l}(r)$ and $P_{n',l'}(r)$ are radial wave functions of the states (n, l) and (n', l') respectively. Gordon (1929) derived the exact expression for the radial integral. The integral contains a hypergeometric function which is difficult to evaluate, especially in the case of high Rydberg states. Hoang-Binh (1990) proposed to make use of a recurrence relation of the hypergeometric function and was able to calculate the hydrogenic radial integrals for principal quantum numbers up to $n \approx 1000$. The algorithm has been publicly available (Hoang-Binh 2005).

APPENDIX C: DEPARTURE COEFFICIENTS

Level population in LTE can be calculated analytically by combining the Saha equation and the Boltzmann equation. At a local temperature T , electron density n_e , and proton density n_p , if assuming LTE, the Saha equation for ionisation fraction reads

$$\frac{n_e n_p}{n_{1s}} = \left(\frac{2\pi m k T}{h^2} \right)^{3/2} \exp(-h\nu_0/kT), \quad (C1)$$

where $h\nu_0$ is the ionisation energy of a neutral hydrogen atom into ionised hydrogen and k is the Stefan-Boltzmann constant. For the level population in an excited state, the Boltzmann equation states

$$\frac{n_{nl}}{n_{1s}} = (2l+1) \exp(-E_{1,n}/kT), \quad (C2)$$

where $E_{1,n}$ is the energy difference between the ground state and the excited state. Combining Equation C1 and Equation C2, the level population in LTE can be written as

$$n_{nl} = (2l+1) \left(\frac{2\pi m k T}{h^2} \right)^{3/2} \exp(E_n/kT) \quad (C3)$$

where E_n is the ionisation potential of the level n and

$$E_n = h\nu_0 - E_{1,n}. \quad (C4)$$

Historically, Menzel (1937) and Menzel & Baker (1937) proposed to express the level population in terms of the dimensionless factor

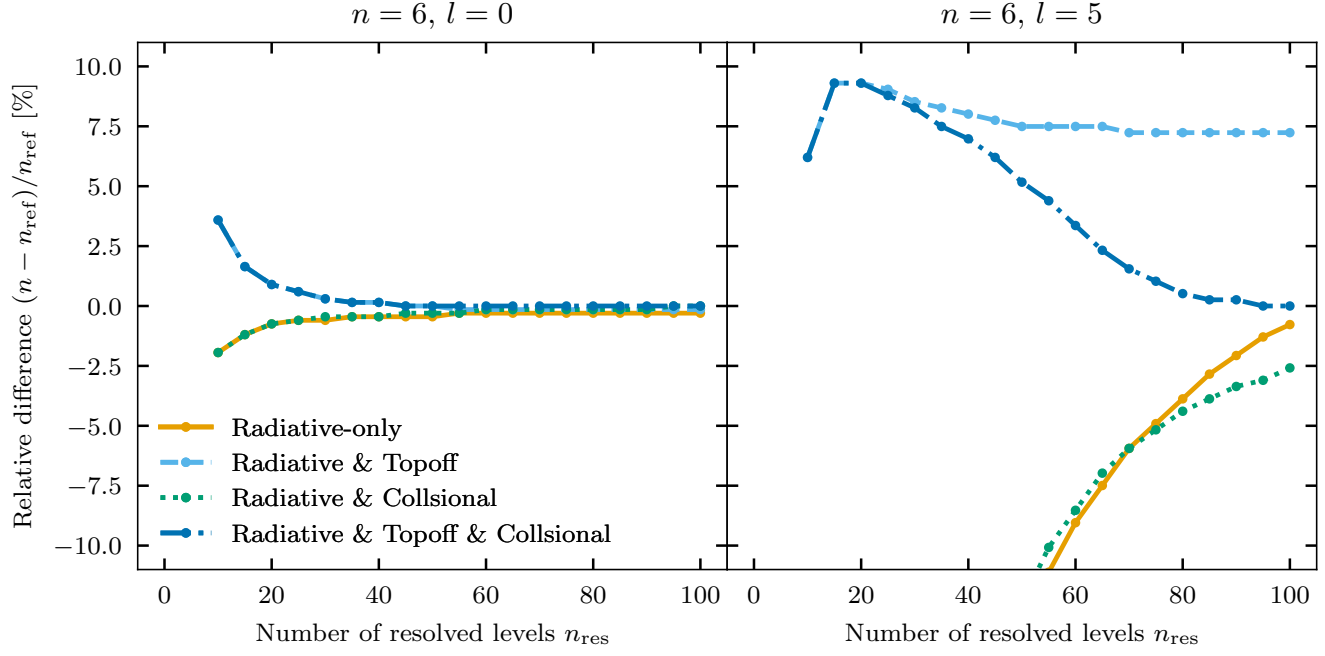


Figure A2. Convergence of level populations predictions in the ‘Ref - ALSH’ model (Table 1) for various settings. The reference model involves 100 resolved and 1 collapsed level, as in all other figures. The vertical axis shows the relative difference between the level populations predicted by different setups and that of the reference model. The ‘Radiative-only’ model takes into account only radiation recombination and radiative cascade. The ‘Radiative & Topoff’ setup includes the conservation of recombination coefficients on top of the ‘Radiative-only’ model, while the ‘Radiative & Collisional’ setup contains collisional processes modelling (collisional excitation, collisional de-excitation, l -changing collision) on top of the ‘Radiative-only’ model. The ‘Radiative & Topoff & Collisional’ setup contains all four processes. Different l -states require different numbers of resolved levels to achieve convergence, and various physical processes have an impact on the convergence.

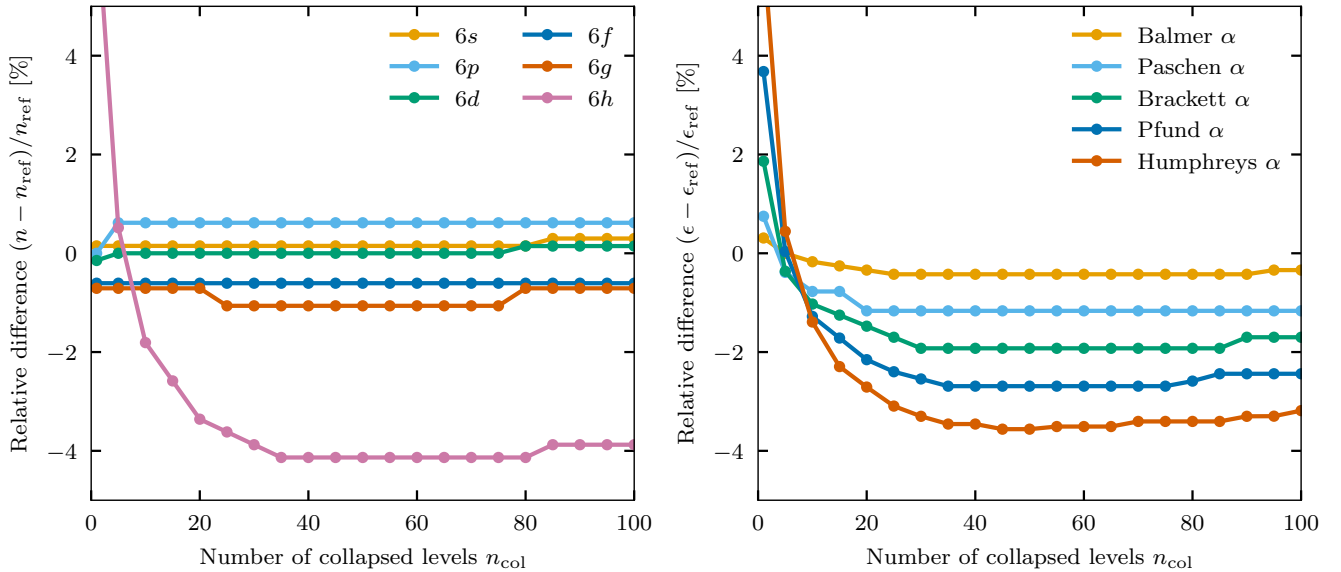


Figure A3. Level population and emissivity predictions from CLOUDY in Case A as a function of the number of collapsed levels for a fixed number of resolved levels of 40. The vertical axis shows the relative difference, either level population (left) or line emissivity (right), between a given setup and the reference setup (‘Ref - ALSH’). Not all l -states in $n = 6$ achieve convergence, even though there are 100 collapsed levels. All the line emissivities are not converged as well, since they are dependent on the level populations.

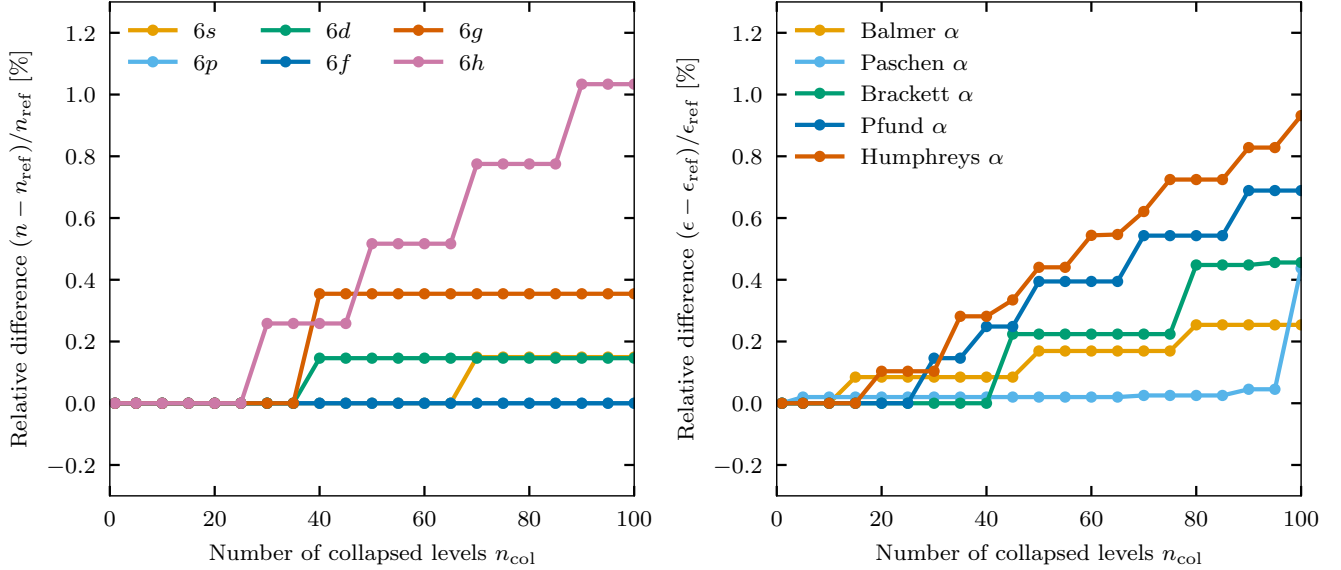


Figure A4. Same as Fig. A3, but with 100 resolved levels.

b_{nl} ¹, often referred to as the departure coefficient, to describe the deviation from LTE. Therefore, in general, the level population is written

$$n_{nl} = b_{nl}(2l+1) \left(\frac{2\pi m k T}{h^2} \right)^{3/2} \exp(E_n/kT), \quad (\text{C5})$$

and $b_{nl} = 1$ is the case where the level population reaches LTE.

Assuming radiative recombination and radiative decays are the only processes that are responsible for setting the level population, i.e., Equation 3 is valid, substituting Equation C5 into Equation 7 gives

$$\begin{aligned} a_{nl} \frac{1}{2l+1} \left(\frac{h^2}{2\pi m k T} \right)^{3/2} \exp(-E_n/kT) \\ + \sum_{n' > n}^{\infty} \sum_{l'} b_{n'l'} A_{n'l',nl} \left(\frac{2l'+1}{2l+1} \right) \exp[(E_{n'} - E_n)/kT] \\ = b_{nl} \sum_{n'=1}^{n-1} \sum_{l'} A_{nl,n'l'}. \quad (\text{C6}) \end{aligned}$$

It is clear that the departure coefficient b_{nl} is independent of density in this case, as used in § 7. However, if we take into account other processes when calculating the level population, e.g., collisional excitation or l -changing collisions, the b_{nl} factor, in general, depends on density (see e.g. Brocklehurst 1971, equation 2.6).

Storey & Hummer (1995) tabulated the intensities of the recombination lines with the disregard of collisional excitation from the ground state, as, in their calculation, they do not predict the population of the ground state and keep it at a sufficiently low level so that collisional excitation from the ground state is negligible (see Hummer & Storey 1987 § 4 and see Storey & Hummer 1995 § 2). Therefore, their tabulated values are only applicable to photon-ionised regions but the partially ionised plasma, e.g., the partially ionised region beyond Strömgren radius in the right panel of Fig. 4. As long as the line emissivity comes from radiative recombination predominantly,

¹ At that time, the model did not resolve l -states.

it is safe to quote their departure coefficients, as are most cases in the literature. The reader should be aware of the subtlety of b_{nl} in this regard.

APPENDIX D: ELECTRON COLLISIONAL EXCITATION RATE COEFFICIENT

In a partially ionised plasma, the collisional excitation from the ground state can alter the population density of the excited states. The ground state is populated much more than any other excited level. Hence, for simplicity, we only model the collisional contribution to the recombination line emissivity from the ground state. In this section, we show how the electron collisional excitation rate coefficients are calculated and how they differ from Raga et al. (2015). In general, our approach follows closely the implementation in CLOUDY. As mentioned in § 3.3, we only consider the collisional excitation from the ground state since the ground state is orders of magnitude more populated than the excited states in the typical condition of an H II region.

For all the levels $n \leq 5$, the Maxwell-averaged effective collisional strengths between the levels, $\Upsilon_{nl,n'l'}$, are given in Anderson et al. (2000) and Anderson et al. (2002) using the R -matrix method. The data is tabulated between electron temperatures 0.5 eV and 25.0 eV. Then we use the standard relation to calculate the collisional de-excitation and excitation rate coefficient, $q_{nl,1}$ and $q_{1,nl}$ (in $\text{cm}^{-3} \text{s}^{-1}$),

$$q_{nl,1s} = \frac{8.628 \times 10^{-6}}{g_{1s} T^{1/2}} \Upsilon_{nl,1s}(T) \exp\left(-\frac{\Delta E_{nl,1s}}{k_B T}\right), \quad (\text{D1})$$

and

$$q_{1s,nl} = \frac{g_{1s}}{g_{nl}} \exp\left(\frac{\Delta E_{nl,1s}}{k_B T}\right) q_{nl,1s}, \quad (\text{D2})$$

where the statistical weight of the ground state is $g_{1s} = 2$. For all the values between the tabulated data points, we use a fifth-order polynomial fit to the effective collisional strength as a function of

temperature, then calculate $q_{nl,1s}$ and $q_{1s,nl}$ using Equation D1 and Equation D2. This polynomial fit also allows us to extrapolate to the lower temperature regime, below 0.5 eV. Note that this approach is slightly different from that in CLOUDY (see § 2.4 of [Lykins et al. 2015](#)). The values for $q_{1s,3s}$, $q_{1s,3p}$, and $q_{1s,3d}$ are shown in the left panel of Fig. D1.

For all the levels $n > 5$, we use the semiclassical straight-trajectory Born approximation proposed by [Lebedev & Beigman \(1998\)](#) to calculate the *ab initio* excitation rate coefficients. This approach is similar to [Guzmán et al. 2019](#). The de-excitation coefficient for $n' \rightarrow n$ is

$$q_{n',n} = \frac{g_n}{g_{n'}} \exp\left(\frac{\Delta E_{nn'}}{k_B T}\right) q_{n \rightarrow n'} = \frac{g_n}{g_{n'}} 2\sqrt{\pi} a_0^2 \alpha c n \left[\frac{n'}{Z(n' - n)} \right]^3 \frac{f(\theta)\psi}{\sqrt{\theta}}, \quad (\text{D3})$$

where

$$\begin{aligned} \psi = & \frac{2n^2 n^2}{(n' + n)^4 (n' - n)^2} [4(n' - n) - 1] \exp\left(\frac{E_n}{k_B T}\right) E_1\left(\frac{E_n}{k_B T}\right) \\ & + \frac{8n^3}{(n' + n)^2 (n' - n) n^2 n'^2} (n' - n - 0.6) \left(\frac{4}{3} + n^2 (n' - n) \right) \\ & \times \left[1 - \frac{E_n}{k_B T} \exp\left(\frac{E_n}{k_B T}\right) E_1\left(\frac{E_n}{k_B T}\right) \right], \end{aligned} \quad (\text{D4})$$

$$f(\theta) = \frac{\ln\left(1 + \frac{n\theta}{Z(n'-n)\sqrt{\theta}+2.5}\right)}{\ln\left(1 + \frac{n\sqrt{\theta}}{Z(n'-n)}\right)}, \quad (\text{D5})$$

$$\theta = \frac{k_B T}{Z^2 I_H}. \quad (\text{D6})$$

In the equations above, α is the fine structure constant, I_H the Rydberg energy, Z the atomic charge of the atom ($Z = 1$ for hydrogen atom), and $E_1(x)$ the first exponential integral (see [Arfken et al. 2013](#)).

Note that there are other methods for calculating collisional excitation coefficients (see [Van Regemorter 1962](#); [Vriens & Smeets 1980](#)), the impact of which on the recombination line emissivity has been studied in [Guzmán et al. 2019](#).

For reference, let us now examine the method proposed by [Raga et al. \(2015\)](#). The temperature dependence of the collisional strengths of the $1 \rightarrow k$ transitions is described by a least-squares polynomial fit of the form

$$\Omega_{1,k}(T) = \sum_{p=0}^5 a_p \log_{10}\left(\frac{T}{10^4 \text{ K}}\right)^k, \quad (\text{D7})$$

where a_p are fitting coefficients, which are given in App. A in [Raga et al. 2015](#). Here, we use a different symbol for the collisional strength only to distinguish different methods. Then the collisional excitation coefficient, $q_{1,k}$, can be calculated from Equation D1 and Equation D2. The total collisional excitation rate coefficient. We compare the $q_{1,3}$ (fitted from [Raga et al. 2015](#)) to that calculated from [Anderson et al. 2000](#) (by summing three components: $q_{1s,3s}$, $q_{1s,3p}$, and $q_{1s,3d}$) in the right panel of Fig. D1 - they are in excellent agreement. In [Raga et al. 2015](#), they consider the l -levels within each n -level to be populated according to their statistical weights, which is inaccurate in typical H II region conditions.

We follow § 3.2.4 in [Hummer & Storey 1987](#) to convert n -resolved collisional excitation rate to nl -resolved, which is slightly different from CLOUDY's implementation (see § 2.4 in [Guzmán et al. 2025](#)).

APPENDIX E: CHOICE OF LASER WIDTH

In this section, we illustrate why we have chosen a laser width of 0.001 throughout this paper. In Fig. 4, we have used a laser beam of 1.1 Ryd with a width of 0.001 to shine on the gas cloud, leading to a very sharp transition between ionised and neutral gas, which is reflected in the sudden drop in $\text{H}\alpha$ emissivity. Increasing the width of the laser will inevitably include Lyman photons that are just below 1 Ryd. These photons have finite optical depths which are close to the continuum optical depth. Such photons from the source will hence be converted to lower-order series, such as $\text{H}\alpha$. More on the finite optical depth of Lyman photons can be found in [Hummer & Storey 1992](#). We illustrate this process by varying the laser widths in Fig. E1. We show the $\text{H}\alpha$ emissivity profile ionized by the same laser with three choices of laser width: 0.001, 0.100, and 0.500. A laser with a larger width will contain more high-order Lyman series and hence be more converted to lower-order series (e.g. $\text{H}\alpha$), resulting in a larger excess in $\text{H}\alpha$ emission beyond the Strömgren radius (~ 1.5 pc).

APPENDIX F: SPECTRUM AND LUMINOSITY FROM PARTICLE DATA

This section outlines our method to estimate the total luminosity of a smoothed-particle hydrodynamic (SPH) snapshot. We illustrate the methodology using $\text{H}\alpha$ as an example. For each particle i in the snapshot, we first calculate the neutral hydrogen mass, $m_{\text{H},i}$, hence the number of hydrogen atoms in that particle, $N_{\text{H},i}$. Our atomic model calculates the level population of individual excited states, e.g. $n_{3s,i}$, $n_{3p,i}$ and $n_{3d,i}$. Then the luminosity of $\text{H}\alpha$ for a single particle i , L_i , can be expressed as

$$L_i = (N_{3s,i} A_{3s,2p} + N_{3p,i} A_{3p,2s} + N_{3d,i} A_{3d,2p}) h v_{3,2}, \quad (\text{F1})$$

where $v_{3 \rightarrow 2}$ is the photon frequency corresponding to the $\text{H}\alpha$ emission. The $N_{3s,i}$ term can be calculated from the integral,

$$N_{3s,i} = \int n_{3s,i} dV = \frac{n_{3s,i}}{n_{\text{H},i}} \int n_{\text{H},i} dV = \frac{n_{3s,i}}{n_{\text{H},i}} N_{\text{H},i}, \quad (\text{F2})$$

where $n_{\text{H},i}$ is the number density of neutral hydrogen in a given SPH particle i and dV is simply the volume element.

We can also calculate the spectrum for each particle. Assuming thermal motion is the only physical process that contributes to line broadening, we can write the line profile $\phi(\nu)$ as

$$\phi(\nu) = \frac{1}{\sigma \sqrt{2\pi}} \exp\left(-\frac{(\nu - \nu_0)^2}{2\sigma^2}\right), \quad (\text{F3})$$

where ν_0 is the central frequency and σ is the dispersion given by:

$$\sigma = \frac{\nu_0}{c} \sqrt{\frac{k_B T}{m_{\text{H}}}}, \quad (\text{F4})$$

where c is the speed of light, k_B is the Boltzmann constant, T is the gas temperature, and m_{H} is the mass of hydrogen atom. Then the luminosity of a particle can be written as

$$L_i(\nu) = L_i \phi(\nu). \quad (\text{F5})$$

Summing over all the particles gives the total spectrum L_{total} :

$$L_{\text{total}}(\nu) = \sum_i L_i(\nu). \quad (\text{F6})$$

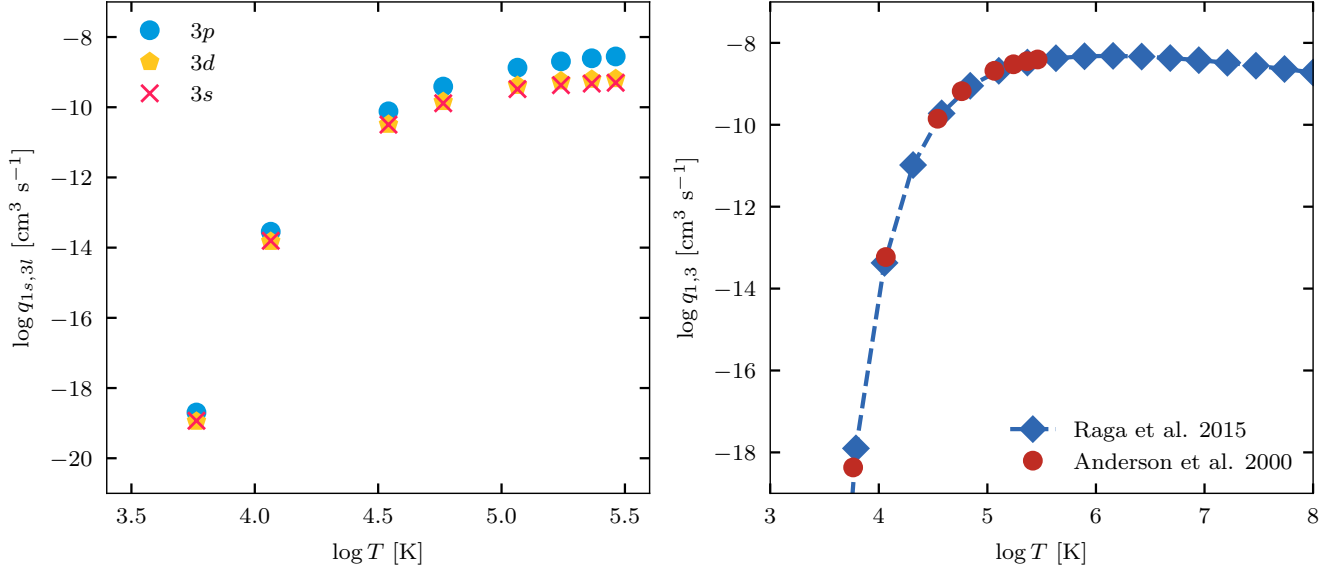


Figure D1. Collisional excitation (by electron impact) rate coefficient as a function of temperature. *Left:* Collisional rate coefficient obtained by Equation D1 with effective collisional strengths listed in Anderson et al. 2000. These rates are l -resolved. *Right:* Comparison of collisional rate coefficient, $q_{1,3}$, between the values used in Raga et al. 2015 and those obtained using Anderson et al. 2000. The $q_{1,3}$ for Anderson et al. 2000 is simply the sum of the three components: $q_{1s,3s}$, $q_{1s,3p}$, and $q_{1s,3d}$. We see excellent agreement between Anderson et al. 2000 and Raga et al. 2015 within the temperature regime that is valid for Anderson et al. 2000.

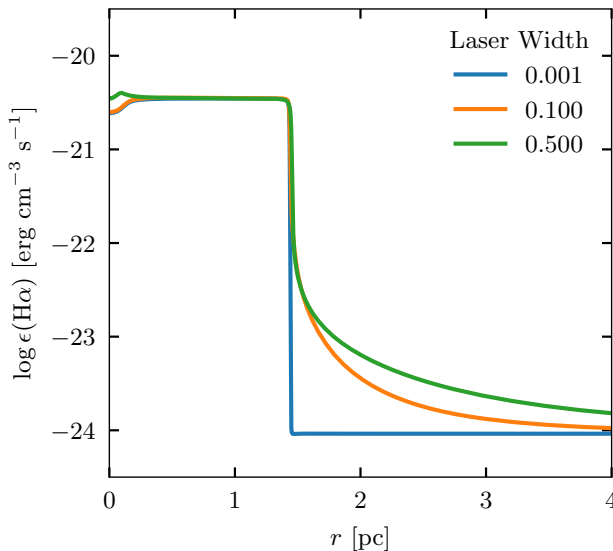


Figure E1. Profile of $\text{H}\alpha$ emissivity, $\epsilon(\text{H}\alpha) \equiv \epsilon_{3,2}$, of a gas cloud ionized by a laser source with different laser widths. We use the setup ‘Ref - LSph’ in Table 1 with varying laser widths. Larger widths lead to the inclusion of high-order Lyman photons which have a finite optical depth. Such photons will hence be converted to low-order series and give rise to the $\text{H}\alpha$ emission.

APPENDIX G: REFINEMENT CRITERION

In our post-processing pipeline, SPH quantities are mapped onto an adaptively oct-tree refined grid that can then be fed into RADMC-3D. The adaptive refinement criterion is set in a way that the smallest grid size, g_{\min} , is a fraction of the minimum smoothing length, denoted by

h_{\min} , of the particles in that grid. The convergence of the refinement choice is shown in Fig. G1, where we post-processed a realistic $\text{H}\alpha$ region with a turbulent density field (see § 4.2.4) with three refinement criteria: $g_{\min} = 1.0 h_{\min}$, $g_{\min} = 0.5 h_{\min}$, and $g_{\min} = 0.3 h_{\min}$. The mock $\text{H}\alpha$ intensity maps in Figure G1 converge in terms of total $\text{H}\alpha$ luminosity, all of which converge to the value calculated from particle, $1.17 \times 10^{35} \text{ erg s}^{-1}$. A more refined criterion (e.g. $g_{\min} = 0.3 h_{\min}$) reveals more small-scale structures. We demonstrate this by examining the $\text{H}\alpha$ intensity along a sightline through the centre of the box ($x = 0.5 \text{ pc}$) in Fig. G2. The intensity fluctuations are more visible in the case of $g_{\min} = 0.3 h_{\min}$, where the dense regions are better refined than the other two cases.

This paper has been typeset from a $\text{TeX}/\text{L}\text{\TeX}$ file prepared by the author.

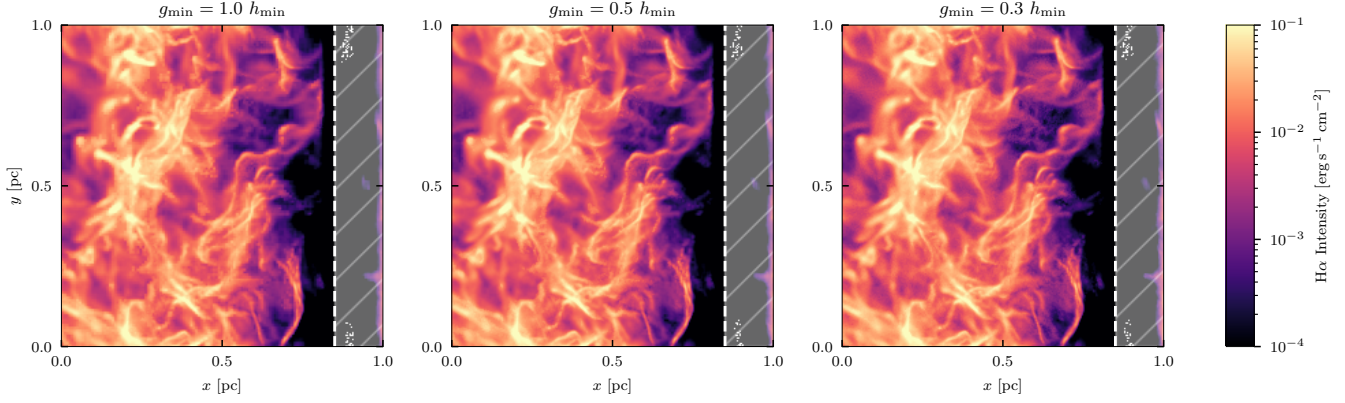


Figure G1. H α intensity maps for different refinement criteria. From left to right, the refinement condition decreases from $1.0 h_{\min}$ to $0.3 h_{\min}$. The total luminosity calculated from the intensity maps converged to the same value, $1.17 \times 10^{35} \text{ erg s}^{-1}$, which is consistent with the value obtained by summing from individual particles. Large-scale structures are similar.

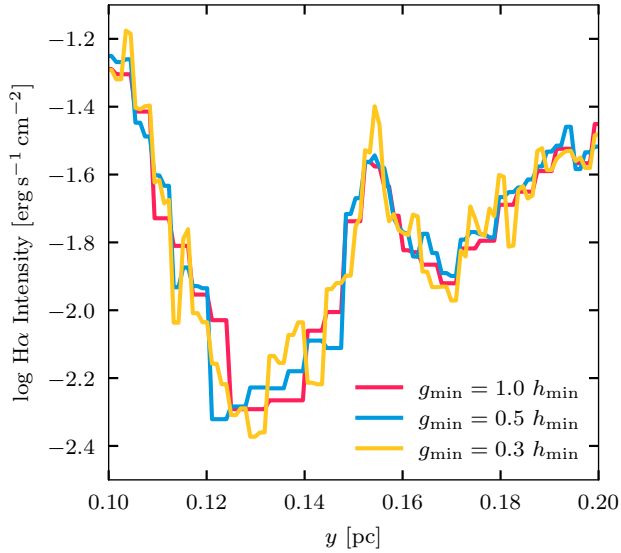


Figure G2. H α intensity fluctuations along the sightline at $x = 0.5 \text{ pc}$ for different refinement criteria. We only show the region $0.1 \text{ pc} < y < 0.2 \text{ pc}$ for simplicity. Intensity fluctuations are more prominent in the case of $g_{\min} = 0.3 h_{\min}$ (yellow line), where the grid is more refined.